Numerical Study of Wind Turbine Wake Aerodynamics in Uniform and Yawed Inflow

Master Thesis

Author(s):
Tsalicoglou, Christina

Publication date:
2012

Permanent link:
https://doi.org/10.3929/ethz-a-010075310

Rights / license:
In Copyright - Non-Commercial Use Permitted

ETH

Eidgenössische Technische Hochschule Zürich
Swiss Federal Institute of Technology Zurich

LEC

Laboratory for Energy Conversion

Christina Tsalicoglou

Numerical Study of Wind Turbine Wake Aerodynamics in Uniform and Yawed Inflow

Master Thesis

Laboratory for Energy Conversion
Swiss Federal Institute of Technology (ETH) Zurich

Tutor

Prof. Dr. Reza S. Abhari

Supervisor

Samira Jafari

April 2012

Acknowledgements

Contents

Abstract

As global wind power capacity increases, wind park power density should be optimized with respect to wind turbine placement and operation. Wake development, interaction and superposition is expected to largely affect power output. Particularly in offshore wind parks, the region downstream of a single wind turbine is dominated by wake effects due to the typically large number of installed wind turbines and low ambient turbulence, which does not facilitate mixing [11], [25].

Detailed understanding of the characteristics of the near wake in non-uniform inflow conditions is necessary both to expand computational tools and to compare with experimental measurements. Therefore the effects of non-axisymmetric, unsteady phenomena on a wind turbine's near wake, up to a distance of two rotor diameters downstream of the rotor plane are presented in this report, in order to create a modeling database to relate the characteristics of a single wind turbine's near-wake to different uniform and non-uniform inflow conditions at various operating points.

Numerical simulations of the turbulent flow downstream of a three-bladed wind turbine are performed by Reynolds-Averaged Navier-Stokes (RANS) modeling, using the commercial code ANSYS CFX 12.1. The simulations are based on the test series of the Model Experiments in Controlled Conditions (MEXICO), performed in 2006 by the Energy Research Center of the Netherlands (ECN) at the German Dutch Wind Tunnels [6].

Simulations are performed for both uniform and non-uniform inflow conditions at three tip-speed ratios $\lambda = 4.17, 6.67$ and 10. The effect of increasing tip-speed ratio and of yawed inflow of $30°$ are studied. Results show good agreement with the experiments. Furthermore, the centerline velocity deficit, trajectory of the tip vortices, wake expansion and flow angles are reported along with the variation of the turbulence kinetic energy across the rotor and at different downstream distances. The extent of the signature of the tower downstream of the wind turbine is also examined for different inflow conditions.

Nomenclature

Symbols

A	rotor swept area	[m^2]
a	axial induction factor	[−]
$a\prime$	angular induction factor	[−]
c_p	power coefficient	[−]
D	rotor diameter	[m]
F_T	thrust	[N]
P	power	[W]
P_0	reference power	[W]
p_{tot}	total pressure	[Pa]
p	static pressure	[Pa]
R	rotor radius	[m]
T	torque	[Nm]
u	velocity	[m/s]
v	velocity in y direction	[m/s]
w	velocity in z direction	[m/s]
u_{ref}	reference velocity	[m/s]
u_∞	freestream velocity	[m/s]
γ	yaw angle	[°]
λ	tip-speed ratio	[−]
ρ	density	[kg/m³]
θ	pitch angle	[°]
ω	rotor rotational speed	[rad/s]

Indices

1	free stream
2	just upstream of the rotor
3	just downstream of the rotor
4	far downstream of the rotor

Acronyms and Abbreviations

2D... nD	positioned at a distance of n times the rotor diameter
BEM	Blade Element Momentum
DT	downstream turbine, usually used for power measurements
TI	turbulence intensity
UT	upstream turbine, usually used for flowfield measurements

Chapter 1

Introduction

1.1 Motivation

In 2008, 81% of the world's energy consumption was covered by fossil fuels - coal, oil and natural gas [1]. However, the variability and the overall increase in the price of fossil fuels over the past years have been making renewable energy sources and nuclear power more competitive. In addition, an increasing awareness of the environmental impact of human activities and a desire for diversification in the energy supply offer further incentives to invest in clean, sustainable energy sources such as the wind. This trend is visible in the global cumulative wind power capacity, which has grown from 6100 MW in 1996 to 238351 MW in 2011 (Fig. 1.1). In 2011, nearly 41 GW of wind power capacity was added around the world and a global capacity of 1000 GW is estimated to be reached by 2020 [10].
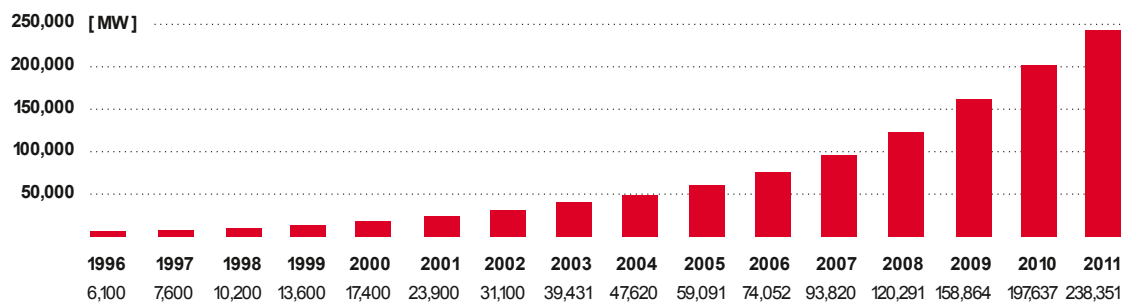
	1996	1997	1998	1999	2000	2001	2002	2003	2004	2005	2006	2007	2008	2009	2010	2011
[MW]	6,100	7,600	10,200	13,600	17,400	23,900	31,100	39,431	47,620	59,091	74,052	93,820	120,291	158,864	197,637	238,351

Figure 1.1: Global cumulative installed wind capacity in the years 1996 to 2011 [10]

As global wind power capacity increases, wind park power density should be optimized with respect to wind turbine placement and operation. The wind characteristics and reliability are significant factors in choosing a site for the construction of a wind park. Wind characteristics mainly depend on the atmospheric conditions and terrain effects. However, wind turbines generate wakes, regions of flow with reduced momentum and

1

increased turbulence, which also take part in forming the inflow conditions for surrounding turbines. Wake development, interaction and superposition is expected to largely affect power output. Particularly in offshore wind parks, the region downstream of a single wind turbine is dominated by wake effects due to the typically large number of installed wind turbines and low ambient turbulence, which does not facilitate mixing of the wake with the freestream [11], [25]. Consequently, turbine placement and operation control in wind parks is a compromise between installing as many machines as possible in a given area while at the same time ensuring that interaction between them is kept to the minimum. [5]

It is therefore necessary for wind park developers to be able to predict quantitatively and with small uncertainties the extent and characteristics of the flow downstream of wind turbines. To reduce computational costs this is done by modeling the expected wake form and its qualities as a function of the inflow conditions and the turbine's operating point. Several models exist to estimate wake development, interaction and superposition. Most of them focus on uniform inflow conditions, as non-uniformity in the inflow results in periodic variations and a three dimensional unsteady wake which is difficult to predict with simplified models [27]. However, a precise knowledge of the effects of unsteady phenomena is of large importance, as wind turbines usually operate in unsteady conditions which may be caused by yaw, shear, the tower shadow, blade flapping or dynamic wind flow. This unsteadiness can significantly change the angle of attack incident at the airfoils , as the rotational speed of wind turbines' rotors is relatively low [21].

The modeling of wind turbines and wake interactions is one of the research topics of the Wind Energy Program of the Laboratory for Energy Conversion (LEC) at ETH Zurich, and has resulted in the development of an immersed boundary and wind turbine model [16]. The present work focuses on the creation of a modeling database to relate the characteristics of a single wind turbine's near-wake to different uniform and non-uniform inflow conditions at various operating points. These results can be further used as boundary conditions in LEC's immersed wind turbine model, thus eliminating the need to resolve the computationally intensive rotor plane for far wake calculations.

Wind park power density should therefore be optimized with respect to wind turbine placement and operation.

1.2   Theoretical Background

The power of an air mass with density ρ flowing at speed u_∞ through an area A can be expressed as

$$P_\infty = \frac{1}{2}\rho A u_\infty^3 \tag{1.1}$$

However, according to Betz's theory, the maximum power that can ideally be extracted from an inviscid free-stream airflow only amounts to 59.26% of P_∞, as the air is decel-

erated when it approaches the rotor plane.

The incoming air flow induces lift forces on the blades of the wind turbine which consequently exert a torque T_{rotor} on the rotor and cause it to rotate with a rotational speed ω, resulting in a mechanical power P_{mech}. The power coefficient is a non-dimensional number which relates the extracted mechanical power to the power available in the undisturbed wind.

$$c_p = \frac{P_{mech}}{P_\infty} = \frac{T_{rotor}\omega}{P_\infty} \tag{1.2}$$

The ratio of the blade tip speed of a rotor of radius R to the free-stream wind speed u_∞ is the tip speed ratio, λ.

$$\lambda = \frac{\omega R}{u_\infty} \tag{1.3}$$

The power coefficient is a function of the tip speed ratio. The optimal tip speed ratio depends on the blade design and on the number of blades of the turbine. For an infinite number of blades, and if the airfoil drag is neglected, the power coefficient reaches the Betz limit as the tip speed ratio increases. In reality, however, there are a finite number of blades so the aerodynamic efficiency of the rotor decreases and tip losses are introduced (Fig. 1.2). Furthermore, the flow is viscous so drag tends to decrease the torque and increase the thrust loading [19, p. 110]. Since drag is proportional to the surface and to the wind speed squared, the power coefficient starts to decrease after a certain tip speed ratio. If, on the other hand, the tip speed ratio is too low the wind passes undisturbed through the blades and almost no power is generated [15, p. 96].
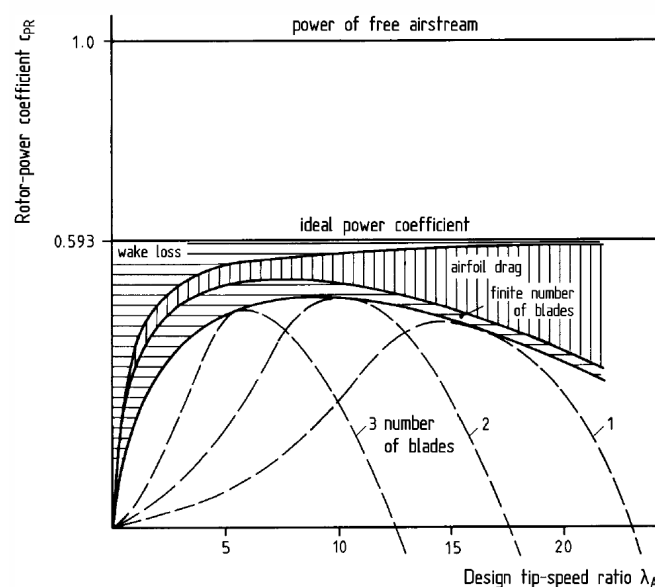

Figure 1.2: Rotor characteristics for ideal and real rotors [15]

To achieve the maximum power extraction the optimum tip speed ratio, λ, which is correlated to a maximum c_p, is defined as a rotor characteristic. Knowing the c_p and the drive train efficiency, η, the mechanical power output of the wind turbine can be predicted as

$$P_{mech} = c_p \eta \frac{1}{2} \rho A u_\infty^3 \qquad (1.4)$$

which results in the characteristic power curve of the wind turbine.

The power curve of a wind turbine relates the electrical power output to the wind speed and is based on the rotor characteristics. This power curve is the most basic tool used to predict the turbine's annual energy production by applying it to a wind speed frequency distribution for the site of interest. However, as other wind flow characteristics such as turbulence fluctuations, shear or misalignment of the wind velocity vector to the rotor influence the power output, the estimation of a wind turbine's performance has to be adjusted to account for such inflow non-uniformities. It is therefore necessary to know both what the inflow conditions to the rotor are as well as what effect they have on power extraction. Theoretical models have been developed to estimate the forces acting on a wind turbine's rotor, the power that can be extracted by it and the form of its wake, which can influence turbines placed downstream. This project focuses on wake characteristics up to a distance of $2\,\mathrm{D}$ downstream of the rotor plane.

1.2.1 Actuator Disk Concept

The basic theory of rotor aerodynamics in based on Betz's Blade Element Momentum (BEM) theory, which models an ideal two-dimensional flow through a rotor disc. The rotor extracts mechanical energy from the flow by reducing its kinetic energy and therefore its velocity. Consequently, if a streamtube is considered, the cross-sectional area through which the flow passes has to increase to ensure the conservation of mass.
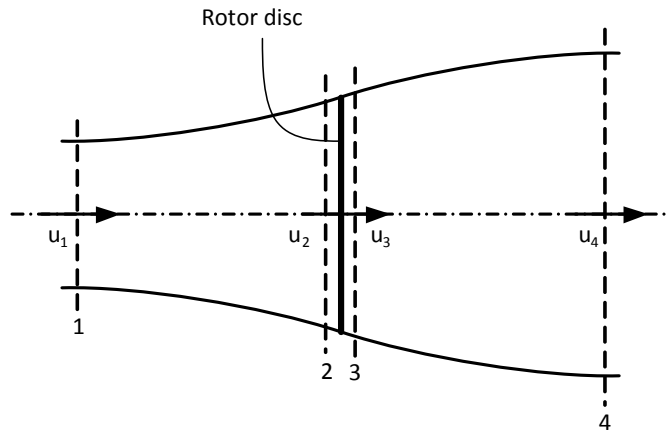

Figure 1.3: Definition of the reference positions used for the Betz analysis

To better describe these considerations four locations of the flow are defined as: 1, free flow, 2, flow just upstream of the turbine rotor, 3, flow just downstream of the turbine rotor and 4, flow far downstream of the turbine rotor (Fig. 1.3, [19, p. 90]). If u_1 is the velocity of the undisturbed flow and u_4 the reduced velocity of the flow far behind the rotor, the area A_4 downstream of the rotor needs to be larger than A_1 in order to maintain a constant mass flow rate $\dot{m}$

$$\dot{m} = \rho u_1 A_1 = \rho u_4 A_4 \tag{1.5}$$

The extracted mechanical power is then given by

$$P = \frac{1}{2}\rho(A_1 u_1^3 - A_4 u_4^3) = \frac{1}{2}\dot{m}(u_1^2 - u_4^2) \tag{1.6}$$

and the thrust acting on the rotor is

$$F_T = \dot{m}(u_1 - u_4) \tag{1.7}$$

As no work is done on the flow on either side of the rotor the Bernoulli equation is valid for the transition from 1 to 2 and 3 to 4 so that the total pressure, p_{tot} of the flow remains constant in these regions, $p_{tot,1} = p_{tot,2}$ and $p_{tot,3} = p_{tot,4}$, with p_{tot} given as

$$p_{tot} = p + \frac{1}{2}\rho u^2 \tag{1.8}$$

By making the further assumptions that $p_1 = p_4$ and $u_2 = u_3$ a new equation can be derived for the thrust, which is ultimately the sum of the forces on either side of the rotor disc $F_T = A_2(p_2 - p_3)$.

$$F_T = \frac{1}{2}\rho A_2(u_1^2 - u_4^2) \tag{1.9}$$

The velocity at the rotor plane can then be found by equating the two given expressions for the thrust. This process results in

$$u_2 = u_3 = \frac{u_1 + u_4}{2} \tag{1.10}$$

The decrease of the wind speed between positions 1 and 2, related to the velocity of the free stream is defined as the axial induction factor, a

$$a = \frac{u_1 - u_2}{u_1} \tag{1.11}$$

The axial induction factor can only vary between 0 and 0.5. With some manipulation of the given equations the power can then be written as

$$P = \frac{1}{2}\rho A_2 u_2 \cdot 4a(1 - a)^2 \tag{1.12}$$

and the resulting power coefficient is

$$c_p = 4a(1-a)^2 \tag{1.13}$$

To maximize the power yield the rotor would have to extract the total kinetic energy of the flow, which would lead the flow to a standstill behind the rotor. This case, however, cannot satisfy the continuity equation as it implies that the velocity u_1 would have to be zero as well. Therefore, the optimal velocity ratio $\frac{u_2}{u_1}$, for which the power is maximized, can be found at $\frac{u_2}{u_1} = \frac{2}{3}$. This yields the optimal $c_{p,max} = 16/27 = 59.26\%$ according to the Betz theory, which is in reality decreased even more due to the rotation of the wake behind the rotor, tip losses on the blades and aerodynamic drag (Fig. 1.2).
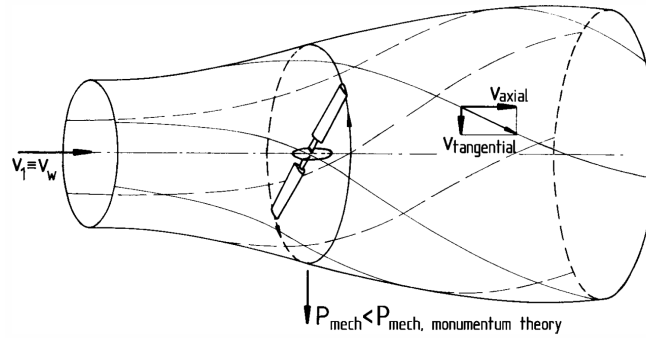

Figure 1.4: Wake rotation in the opposite direction of the blades [15]

In reality the rotor, rotating with ω, imparts a tangential velocity component to the flow, causing the wake behind it to rotate in the opposite direction, with angular velocity ω_2 in order to maintain the angular momentum (Fig. 1.4). The angular induction factor $a\prime$ is then defined as

$$a\prime = \frac{\omega_2}{2\omega} \tag{1.14}$$

Tip vortices

Corrections to the original Blade Element Momentum Model account for tip vortices, which occur due to the pressure difference between the blade's pressure and suction side. Tip vortices play an important role in the velocity distribution at the rotor. Prandtl's theory models the helical vortices as vortex sheets convected by the mean flow. However, this model's accuracy decreases for rotors with fewer blades and higher tip speed ratios [22].

Generally, according to the Kutta-Jukowski law the lift, L, generated by a blade is equal to

$$L = \rho u_\infty \Delta\Gamma \tag{1.15}$$

, where $\Delta\Gamma$ is the strength of the bound vortex. For a three-bladed wind turbine one tip vortex of strength $\Delta\Gamma$ is generated by each airfoil and a root vortex of strength $3\Delta\Gamma$ is generated at the hub. As the wake rotates opposite to the rotor's rotational speed the tip and root vortices are convected downstream along helical paths [24].

Correction for yawed inflow

When the inflow to the rotor is not axisymmetric, in cases where the wind turbine operates in yaw, the resulting wake is also skewed relative to the incoming flow axis. This affects the induction factor, which is calculated as

$$a_{yaw} = a(1 + K\frac{r}{R}\cos\psi) \tag{1.16}$$

where a_{yaw} is the induction factor for the yawed inflow, K is a factor of the yaw angle, r the radial position, R the rotor radius and ψ the azimuth angle which is zero for the most downwind position relative to the inflow [22].

Furthermore, the angle χ of the wake relative to the rotor axis is found to be larger than the angle γ of the incoming yawed flow (Fig. 1.5). The basic formula is derived by Coleman et al. [9] as

$$\tan\chi = \frac{u_\infty(\sin\gamma - a\tan\frac{\chi}{2})}{u_\infty(\cos\gamma - a)} \tag{1.17}$$
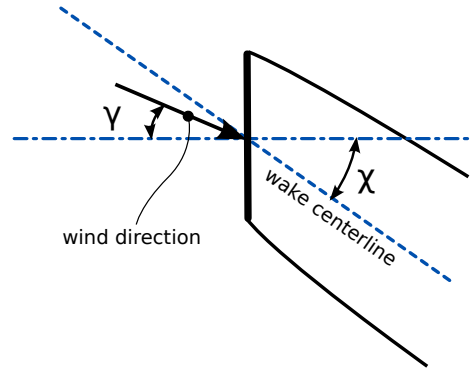
where a is the axial induction factor.

Figure 1.5: Wake orientation for a wind turbine operating under yaw. The yaw angle, γ is smaller than the skew angle of the wake, χ, relative to the rotor plane.

1.2.2 Wake Modeling

Near wake

The near wake is defined as the area shortly downstream of the rotor where the properties of the rotor, such as the number and aerodynamic properties of the blades 3D effects

and tip vortices, are still discernible [27]. The definition of the actual distance varies in literature from 1 D [27] to 3-5 D [2].

Due to the velocity deficit the wake expands within the near wake region but a recovery of the velocity occurs as the slow flow inside the wake mixes with the fast freestream flow. The difference in the velocity between the air inside and outside of the wake results in a shear layer of higher turbulence intensity, which contributes to momentum transfer from the high speed region to the wake. When the ambient turbulence is lower, such as in offshore wind parks, the wake recovery occurs over a longer distance. Tip vortices and turbulent boundary layers also contribute to increasing the turbulence within the wake and reinforce mixing.

Existing wake models

Wake models approximate the wake's qualities by making assumptions concerning the representation of the turbine, the evolution of the velocity profile, the turbulence distribution, and the description of the boundary layer. The models can either be based on self-similar velocity deficit profiles developed for co-flowing jets, in which case they are called kinematic models, or they may solve the simplified momentum equations for every point in the flow field, and are then termed field models [11]. As kinematic models use self-similar velocity profiles, they are only valid for describing the far wake, where the signature of the rotor and tower are no longer evident in the flow.

Well-known kinematic models include the wake model by Jensen [18], the Risoe WAsP and analytical model and the Uo FLaP model. The model by Jansen assumes a top-hat shape for the shape of the velocity deficit in the wake (Fig. 1.6). However, a bell-shaped or Gaussian distribution has been shown to deliver more accurate results. Moreover, the Risoe WAsP model is based on the model by Jensen [18] and assumes linear expansion of the wake with symmetric width in the vertical and lateral directions [3]. The Risoe analytical model is based on the conservation of the momentum deficit downstream of a wind turbine, assuming that there is no reason for losses other than the turbine itself. Furthermore, the UO FLaP model [20] starts calculation at the end of the near wake and assumes axisymmetric incompressible flow without pressure gradients. An empirical wake profile is used as initial conditions for the beginning of calculations.

Field models may make assumptions such as two-dimensional flow, axisymmetric flow, isotropic turbulence, or may neglect in-plane pressure gradients in order to simplify the momentum equations and reduce computational time [11]. As such assumptions are best valid in the far wake, where the signature of the rotor is not significant, results from these methods match best for the far wake region. An approach developed by Cleijne and Voutsinas [8], [28] separates the wake into a rotor region, a near-wake region and a far wake region and applies different solution methods to each region.
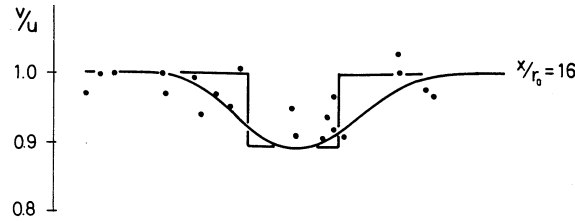
Figure 1.6: Top-hat shape of the velocity deficit according to the jensen model. The experimental values, noted by the points are better approximated by a bell distribution [18].

1.2.3 Full rotor simulations

Computational Fluid Dynamics methods solve the three dimensional incompressible Navier-Stokes partial differential and continuity equations for the flow field around a wind turbine.

$$\frac{\partial \vec{u}}{\partial t} + (\vec{u}\nabla)\vec{u} = -\frac{1}{\rho}\nabla p + \nu\nabla^2\vec{u} \tag{1.18}$$

$$\nabla\vec{u} = 0 \tag{1.19}$$

where $\vec{u}$ is the velocity vector, t the time, and p the pressure. For wind turbines, the Reynolds number, Re, which appears in the non-dimensionalized the Navier-Stokes equations, is defined based on the chord length of the blade, c, at each spanwise position, and the azimuthal velocity of the blade, ωr. This results in $Re = \frac{\omega r c}{\nu}$ in the order of 10^6 for large turbines, where ω is the rotational speed of the rotor, r the radius and ν is the kinematic viscosity. Due to the turbulent nature of the flow, small-scale structures in the order of η $Re^{-3/4} \cdot c$, where c is the characteristic length and η the length of the smallest scales, at which the viscous effects become dominant and the energy is dissipated [17].

As these very small scales would need to be resolved in order to directly solve the equation system by Direct Numerical Simulation (DNS), a very fine grid would be necessary, which would result in a very large computational time. Therefore, the fluctuations of the turbulent quantities are averaged, which results in an system with more unknowns than equations, due to the fact that the Navier-Stokes equations are not linear in the velocity. This introduces a closure problem, which calls for the modeling of the additional terms that arise due to averaging.

Two of the most widely used models are the two-equation $k - \epsilon$ and $k - \omega$ models [30], which are both based on the Boussinesq hypothesis that the Reynolds stresses are linked to the velocity gradients by a turbulent viscosity, ν_t. The models introduce two additional transport equations, one for the turbulent kinetic energy, k and one for the turbulent dissipation ϵ or the specific dissipation rate $\omega \sim \frac{\epsilon}{k}$ respectively.

The advantage of the $k-\omega$ model compared to $k-\epsilon$ is a better performance for calculating

the boundary layer, especially under adverse pressure gradients. However, this model is very sensitive to the value of ω in the free stream and the solution may be significantly affected by the free-stream turbulence properties at the inlet. Therefore, the SST model combines the two approaches by implementing the $k - \omega$ model in the near wall region and switching to $k - \epsilon$ for calculating the free stream properties [23] .

1.2.4   Challenges in Unsteady Aerodynamics

Wind turbines are generally subjected to atmospheric variations and must, therefore, operate in a complicated unsteady environment. Some of the environmental effects that affect their operation include atmospheric turbulence, shear effects due to the ground boundary layer, directional variation of the inflow direction or a temporally variable inflow due to influence by another turbine's wake [21]. Unsteady inflow variations result in off-design structural loads and aerodynamic forces. When the inflow velocity over the rotor area is not uniform each blade segment operates under different conditions depending on the rotor's position, which consequently affects the flow downstream of the turbine as form a three-dimensional, unsteady wake. One of the most widespread ways of modeling such wake structures are vortex wake models, where the circulation strength and the positions of the shed vortices can be evaluated (Fig. 1.7). However, the repeated evaluation of the Biot-Savart law for evaluating the characteristics of the tip vortices requires large computational effort. Methods developed to reduce computational effort result in instabilities in the solution, which are difficult to discern from instabilities that may be caused from the inherently unstable nature of the problem. Moreover, comparison with full scale measurements prove to be a challenge, as the inflow conditions are not easily defined.
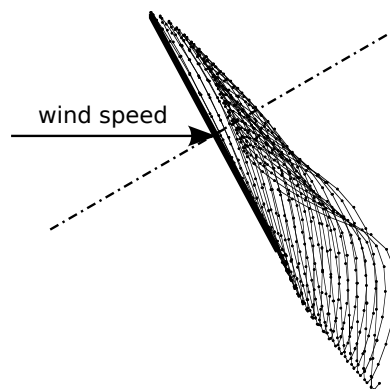

Figure 1.7: Time-accurate free vortex wake calculation of a three-bladed wind turbine operating at 30° yaw and a $15\,\mathrm{m/s}$ wind speed [21].

Chapter 2

Computational Setup

Results derived from numerical simulations require experimental validation to verify their accuracy and to identify possible errors in the modeling of the problem. In this project CFD (Computational Fluid Dynamics) results are compared with experimental data from wind tunnel tests performed in the Large Scale Low Speed Facility (LLF) of the German-Dutch Wind Tunnels (DNW). The data are derived from a series of experiments coordinated by the Energy Research Center of the Netherlands (ECN) under the name MEXICO (Model Rotor Experiments under Controlled Conditions) [6]. The experiment was executed in 2006 and its main objective was the creation of a database of aerodynamic measurements under known conditions for use in CFD computations.

2.1 The MEXICO Experiment

The LLF wind tunnel has an open test section of $9.5 \times 9.5\,\mathrm{m}^2$ (Fig. 2.1). The flow is blowing from a nozzle to a collector through a closed loop [6]. The turbulence intensity in the tunnel is 0.8% in the longitudinal direction, and 0.16% in the lateral direction. The wind turbine's rotor has 3 blades and a diameter of 4.5 m resulting in a rotor swept area of $15.9\,\mathrm{m}^2$ and a blockage ratio of 18% in the wind tunnel. Blockage effects were observed in the far wake of the turbine, where a speed-up of the flow was noted close to collector. However, it has been confirmed by simulations that the blockage does not significantly affect the induction in the rotor plane and the near wake [26]. The rotor's speed is 424.5 rpm and it rotates in the clockwise direction. Finally, the tower is mounted on a base that can rotate in order to simulate yawed inflow conditions.

The measurements performed include pressure measurements at five different positions of the blades, moments and forces at the foot of the tower, and flowfield PIV measurements to capture the induced 3D flow at one diameter (1 D) upstream and downstream of the rotor.
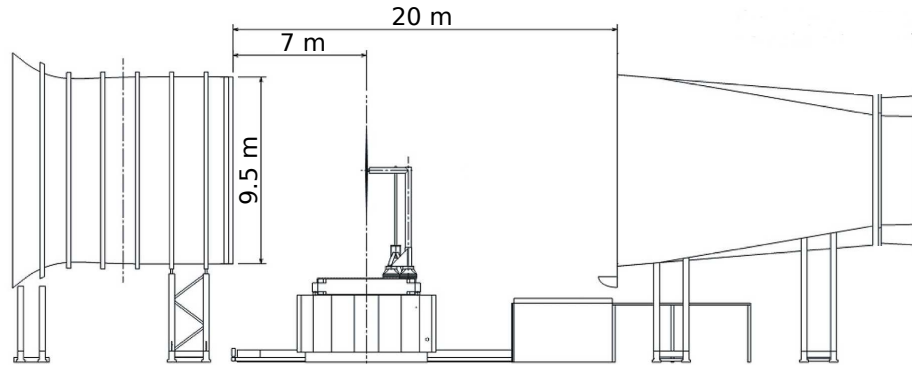
Figure 2.1: Setup and dimensions of the LLF wind tunnel, used for conducting the MEXICO experiment [6].

The aim of the project was the creation of a well documented database of aerodynamic measurements, which are taken under controlled and therefore known conditions, and which can be used to validate or improve computational methods (BEM methods, free wake calculations and CFD simulations) [6].

The three-dimensional flow field measurements were performed using Particle Image Velocimetry (PIV) with small bubbles used as seeding particles. Two cameras were aimed at a horizontal PIV sheet which was illuminated by a laser flash and they took two photographs with a delay of 200 ns. The velocity vector in PIV results from the maximum cross correlation between two sequential photographs.

A large number of different operating conditions were tested with different wind speeds, yaw angles, blade pitch angles and rotor rotational speeds. The cases which are of interest for this project include cases with uniform inflow at three different wind speeds of $10\,\mathrm{m/s}$, $15\,\mathrm{m/s}$, which is the operating point for the given rotor and rotational speed, and $24\,\mathrm{m/s}$. These speeds correspond to tip speed ratios $\lambda = 10, 6.67$ and 4.17 respectively. Moreover, the $30\,^\circ$ yawed case at $\lambda = 6.67$ is used to validate the yawed simulations.

2.2   Wind Turbine Model

To be able to correctly compare the simulations to the measurements the exact geometry of the MEXICO experiment wind turbine is used for the numerical simulations. The rotor diameter is $4.5\,\mathrm{m}$ and the blade length is $2.04\,\mathrm{m}$, as the spinner has a diameter of $0.42\,\mathrm{m}$ (Fig. 2.2). The tower height is at $5.3\,\mathrm{m}$ above ground and the tubular tower has a diameter of $0.5\,\mathrm{m}$. The complete $360\,^\circ$ of the rotor and the tower are included in the computational domain.

The blade geometry of the wind turbine is a combination of three different airfoil families. These are the DU91-W2-250 at the blade root, the RISØA1-21 at mid-span and the

NACA64-418 profile at the outer part of the blade, with transition zones between these parts [6]. The blade pitch angle is set at $-2.3°$. Details of the geometry such as the base on which the turbine stands and roughness elements located on the blades and tower, used to provoke transition to turbulence, have been committed. Blockage effects from the tunnel have also been neglected.
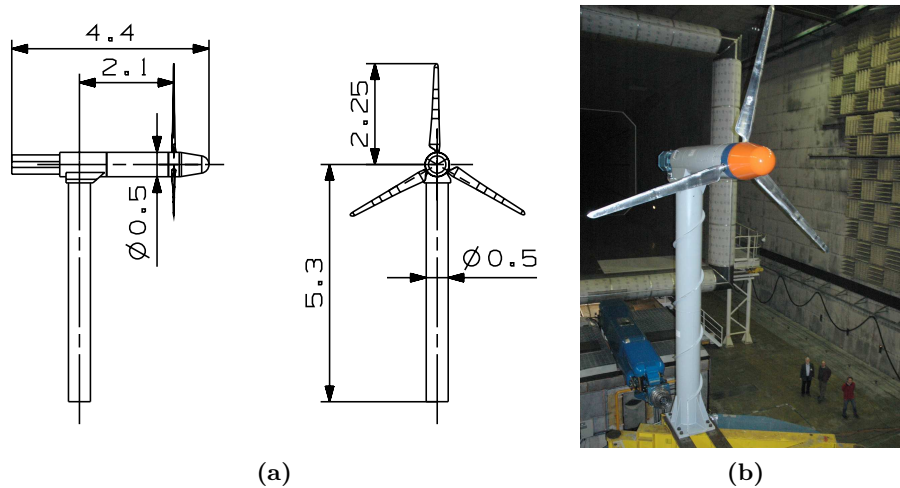

Figure 2.2: Wind turbine used in the MEXICO experiment and modelled for the CFD simulations of the present work (a) and wind turbine in the LLF wind tunnel (b).

2.2.1 Computational Domain and Setup

The computational domain is spherical and has its outer boundary seven rotor diameters, $7\,D$, away from the wind turbine. A spherical computational domain was chosen to allow an easy adjustment of the inflow direction, and to facilitate the testing of cases with yawed inflow without extensive modification of the setup or mesh. However, numerical errors introduced when specifying non-uniform or non-axisymmetric inflow conditions on a rotating domain have enforced the diversification of the domain setup for uniform and non-uniform cases. The domain is always separated by a fluid-fluid interface in one sub-domain which is solved in the stationary frame of reference and includes the stationary parts of the turbine and one which is solved in the rotating frame of reference and includes the rotor. The different set-ups used are described in the following section. All numerical simulations carried out for this project are done using the commercial software ANSYS CFX 12.1.

Three set-ups are used, with the coordinate system always specified as in Fig. 2.3:

(a) Uniform inflow, tower included

The wind turbine, including the rotor, nacelle and tower, is placed in the middle of the spherical domain. The domain is separated by the YZ-plane crossing the

point $(0,0,0)$ into two hemispheres which define two separate domains. The inlet boundary is specified on the surface of the front hemisphere (in +X) and the outlet on the surface of the rear hemisphere. The front domain contains the rotor and half of the nacelle and the rear the tower and the other half of the nacelle. The front part is solved in a rotating frame of reference in order to simulate the wind turbine's rotation while the rear is solved in a stationary frame of reference. The plane separating the two hemispheres is specified as a fluid-fluid frozen-rotor interface between a stationary and a rotating domain. This setup is used for testing axisymmetric and uniform inflow conditions (Fig. 2.3)
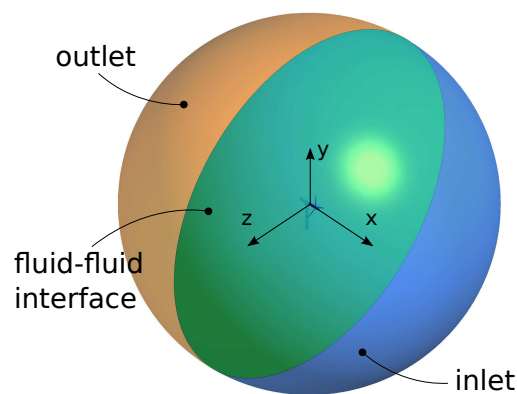

Figure 2.3: Basic setup, including the tower and used for uniform inflow conditions.

(b) Non-uniform inflow, tower included

For simulations in yaw or shear, the inlet boundary condition must necessarily be specified on a surface that is in a stationary domain. Else, pressure gradients of the order of $500\,\mathrm{Pa/m}$, which disrupt the flow, occur in the domain. A solution to this problem while using the same setup was not found during this project despite extensive communication with the software's support, who ultimately confirmed the problem. Therefore, the domain used for the cases with non-uniform inflow is altered as follows so that the inlet surface is part of a stationary domain.

The wind turbine, including the rotor, nacelle and tower, is placed in the middle of the spherical domain. A small cylinder around the wind turbine rotor specifies the rotating domain while the rest of the domain is solved in the stationary frame of reference. The surfaces of the cylinder constitute the fluid-fluid interface. The diameter of the inner cylinder is $1.3\,\mathrm{D}$ and its length is $0.67\,\mathrm{D}$, with the rotor located in the middle (Fig. 2.4a). The inlet and outlet surfaces are rotated by the yaw angle around the y-axis so that the velocity vector at the inlet can be normal to the inlet surface.

(c) Uniform inflow, tower not included

The previously described set-ups allow the inclusion of the tower. However, as the tower is not rotationally symmetric it has to be in a stationary domain. Therefore,
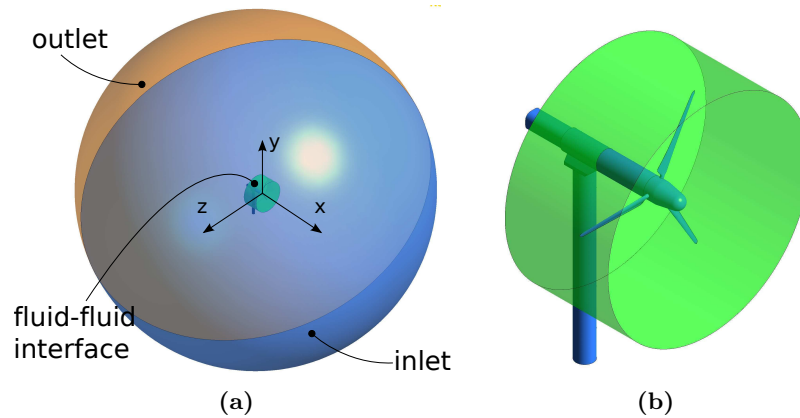
Figure 2.4: Setup for simulations with non-uniform inflow 2.4a and close-up of the wind turbine with the surrounding cylinder 2.4b

the interface between the rotating and the stationary domain has to be placed at most at $0.3\,\mathrm{D}$ downstream of the rotor, as the tower is located at about $0.4\,\mathrm{D}$ downstream of the rotor. To avoid any impact that the fluid-fluid interface may have on the flow field it is preferable to locate the interface as far as possible from the rotor. Furthermore, as the computational capacity is limited, including the tower results in a larger number of nodes which could otherwise be used to increased the mesh density in the wake region. Therefore, the following setup where the tower is neglected and the interface is placed further away from the turbine, is used increase the resolution in the wake, minimize the effect of the interface and have a point of reference against which to compare other results.

The wind turbine, including the rotor and nacelle but not the tower, is placed in the middle of the spherical domain, which is separated by the YZ-plane crossing the point $(0, 0, 0)$ into two hemispheres which define two separate domains. The rotor is placed two rotor diameters upstream of the fluid fluid interface. The fluid-fluid interface and inlet and outlet boundaries are specified as in case (a) (Fig. 2.3)

In all cases the velocity in cartesian components is specified at the inlet and the static pressure at the outlet. The air density, static pressure and temperature are specified according to the conditions indicated and used by the MEXICO experiment. The SST turbulence model is used as it combines advantages of both the $k - \epsilon$ and the $k - \omega$ models, as described in section 1.2.3.

2.3 Computational Mesh

Several mesh types have been used with node counts ranging from 13×10^6 to 19×10^6. The meshes for which the final results are presented in this report have 15.5×10^6 nodes

for the setup case (a), 19×10^6 for case (b) and 15×10^6 for case (c). All volume meshes used are unstructured and generated with the Octree algorithm of the meshing software ICEM CFD of ANSYS (Fig. 2.8). In order to resolve the boundary layer 25 prisms layers are placed adjacent to all wall boundaries (Fig. 2.6). To keep the y+ value below 2 on the blade surface the height of the first prism layer is 1×10^{-5} m. The expansion ratio is 1.3 and following the exponential growth law it results in a total height of 23 mm for the 25 layers, which is about 70% of the blade thickness at mid-span. The surface mesh on the blades has 600 nodes in the spanwise direction and 55 nodes in the chordwise direction at mid-span (Fig. 2.5).
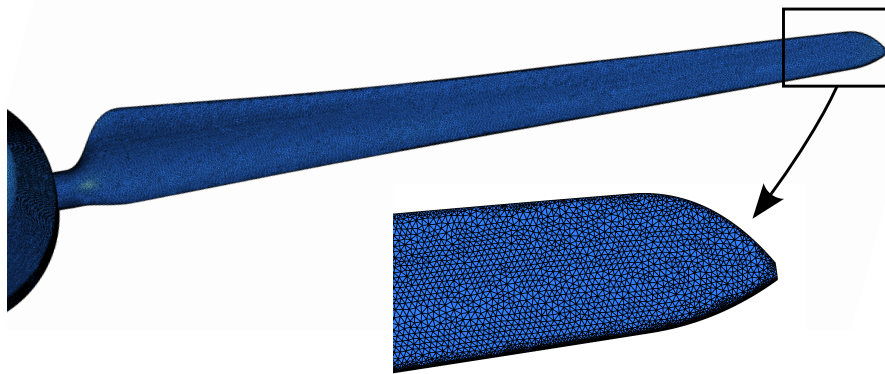

Figure 2.5: Surface mesh on rotor blade.

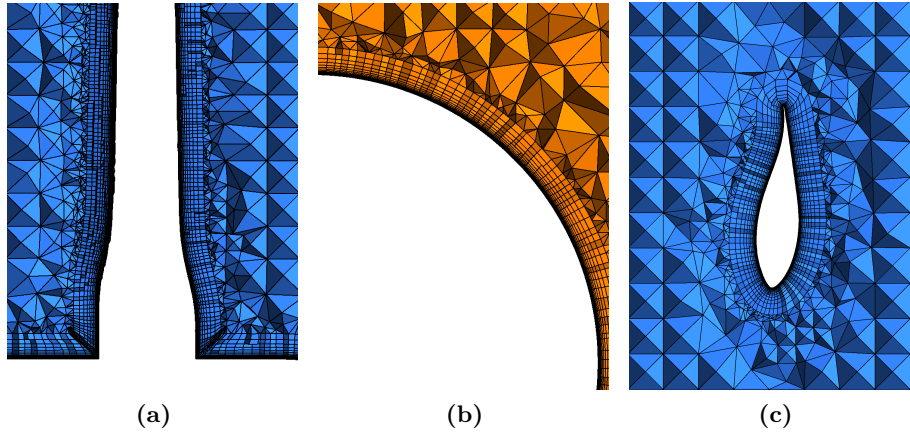(a)   (b)   (c)

Figure 2.6: Prism layers around the hub (a), the tower (b), and blade at mid-span (c) .

To reduce the total number of nodes and consequently the computational time and required memory, both to generate the mesh and to calculate the numerical solution the mesh is more refined close to the wind turbine and coarser away from it. Using a spherical domain results in a large volume which is filled initially with coarse elements. Closer to the turbine and in the region where the wake is expected to evolve the mesh

is refined. This is also one reason why different meshes should be used for axial and yawed inflow, as it is important to optimally distribute the finer elements. The finer mesh region reaches up to 2 D and beyond that distance coarsening compromises the accuracy of the numerical solution. Good agreement with experimental values confirm that the grid coarsening beyond 2 D does not affect the flow field up to that point.

For the setup used for the non-uniform inflow conditions, where a cylinder defines the fluid-fluid interface close to the blades (Fig. 2.4b) the mesh around the wind turbine is as fine as for the case with no tower. Trials have shown that this is necessary in order to reduce the possibility of the interface influencing the flow, being so close to the rotor. A very fine mesh near the rotor and the inclusion of the tower impose the need to begin grid coarsening further upstream, so in this case the results should only be trusted until 1.5 D, where the mesh begins to coarsen. Finally, the region of high density is oriented in the direction where the wake is expected to evolve under these conditions, so that a different mesh must necessarily be used for uniform and non-uniform conditions if an optimal allocation of fine elements is desired.
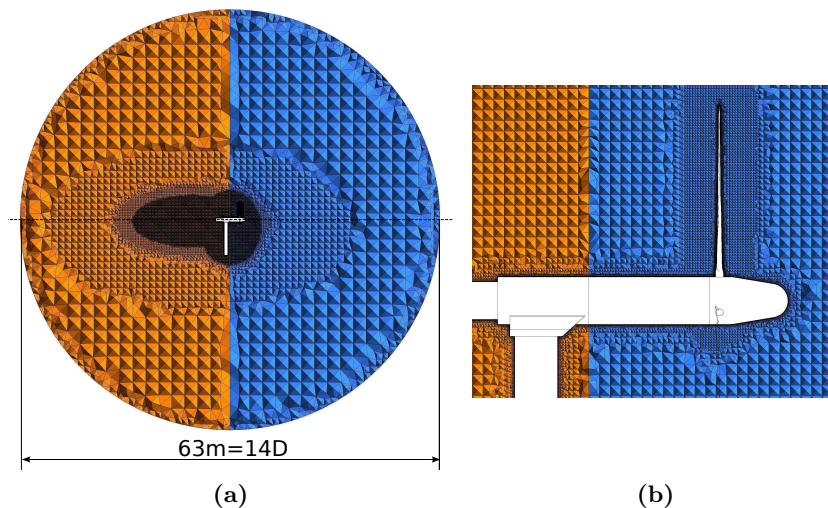

(a)   (b)

Figure 2.7: Unstructured Octree-type volume mesh (a) and closer view of the mesh around the wind turbine (b).

2.4   Convergence

Convergence of the simulations was certified by monitoring the RMS values of the momentum equations for the velocity components and the pressure equation. Additionally, the torque and as well as downstream velocities and pressures at 1 D and 2 D were monitored. The mesh was refined until the torque estimated between two subsequent mesh resolutions remained unchanged and characteristic flow values were consistent with experimental results.
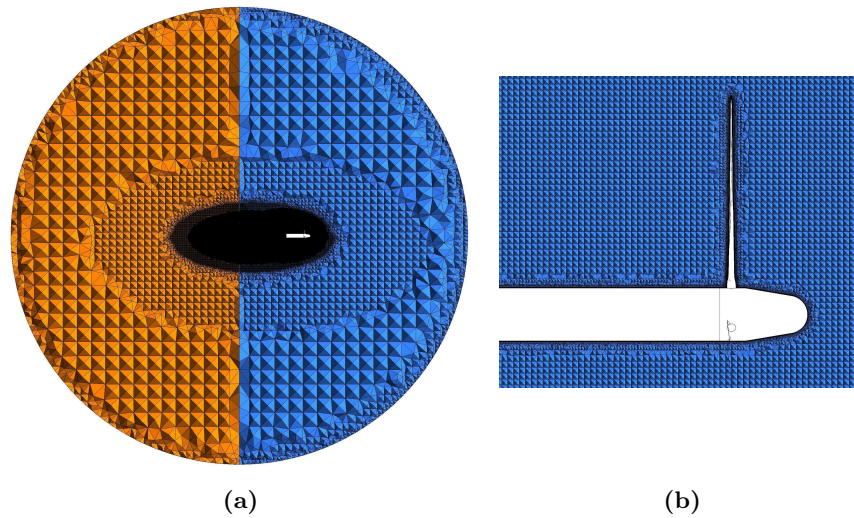
(a)   (b)

Figure 2.8: Unstructured Octree-type volume mesh (a) and closer view of the mesh around the wind turbine (b) for the case without a tower and finer grid resolution.

The timestep option was chosen as "automatic" by ANSYS CFX and adapted by scaling to reach convergence. For lower tip speed ratios a higher scaling factor of the automatic timestep is necessary to minimize fluctuations of the values at the monitoring points and of the error equations' RMS values. This is because the frequency of unsteady vortex shedding increases with increasing speed, so the period reduces and even small time steps do not capture the temporal variation of the flowfield values. On the other hand, when a small time step is used at low velocities the iteration at each time step sees an evolving time-dependent flow, causing large errors in the equations's residuals.

At convergence, the RMS values lay at approximately 5×10^{-5} for the momentum equations and at 5×10^{-8} for the pressure equations. Some fluctuations of the order of 10^{-5} remain for the residuals, even at convergence, due to the unsteady vortex shedding at the tower. These fluctuations vanish for the cases where the tower is omitted, validating the assumption that they are caused by the tower shedding.

Chapter 3

Results and Discussion

3.1 Uniform Inflow Conditions

3.1.1 Rotor Aerodynamics

The torque, thrust and pressure distribution along the blades are calculated for three different wind speeds of 10, 15 and 24 m/s. As the rotational speed is $\omega = 44.5\,\text{rad/s}$ and the radius is $R = 2.5\,\text{m}$ this corresponds to tip-speed ratios $\lambda = 10, 6.67$ and 4.17 respectively, with the operating point being at $\lambda = 6.67$. The computational set-ups which are compared include the three cases described in section 2.2.1, with two different mesh resolutions, a coarse and a finer one used in the standard setup, (a), to confirm the grid independency.

The predicted pressure coefficients are compared with experimental values at five different spanwise positions for all three tip-speed ratios. The pressure coefficient is calculated as

$$c_P = \frac{p - p_{ref}}{\frac{1}{2}\rho W^2}, \qquad W = (\omega r)^2 + u_{ref}^2 \tag{3.1}$$

where p is the pressure, p_{ref} the ambient pressure, ρ the air density, and W the relative velocity that a blade portion at radius r would see in a flow field with freestream velocity u_{ref}, as it rotates with the angular velocity ω. The results for the standard setup with a fine mesh show good agreement with the experiments (Figs. 3.3, 3.2, 3.1). The difference from the experimental values, averaged over all five spanwise positions, is 17%, 9% and 8% of the local dynamic pressure for $\lambda = 4.17$, 6.67 and 10 respectively. The largest discrepancy from the experimental values is observed at the 25% spanwise position on the suction side for $\lambda = 4.17$, where it amounts to 60%. This large difference may be attributed to underestimated separation close to the hub, as the rotor is not operating at its design point. Small discrepancy is observed between the values calculated with the different set-ups (Table 3.1). In general the pressure coefficient is approximated better for

the pressure side, where the flow follows the pressure gradient and for the outer spanwise locations, as there is a smaller possibility for separation in the outer portion of the blade, which is usually aerodynamically optimized. Furthermore, mismatch for the 25% and 35% spanwise positions in the results for $\lambda = 10$ may be caused by faulty measurements, as has been noted Bechmann et al [5], who also worked on CFD simulations of the MEXICO rotor.

setup and mesh	$\lambda = 4.17$	$\lambda = 6.67$	$\lambda = 10$
standard, fine	17.6%	9.3%	8%
standard, coarse	17.3%	9.6%	8%
no tower	17.5%	9.5%	8.1%
rot. cylinder	-	9.2%	-

Table 3.1: Difference between the predicted pressure coefficients and experiments values as percentage of the local dynamic pressure, for the different computational set-ups.
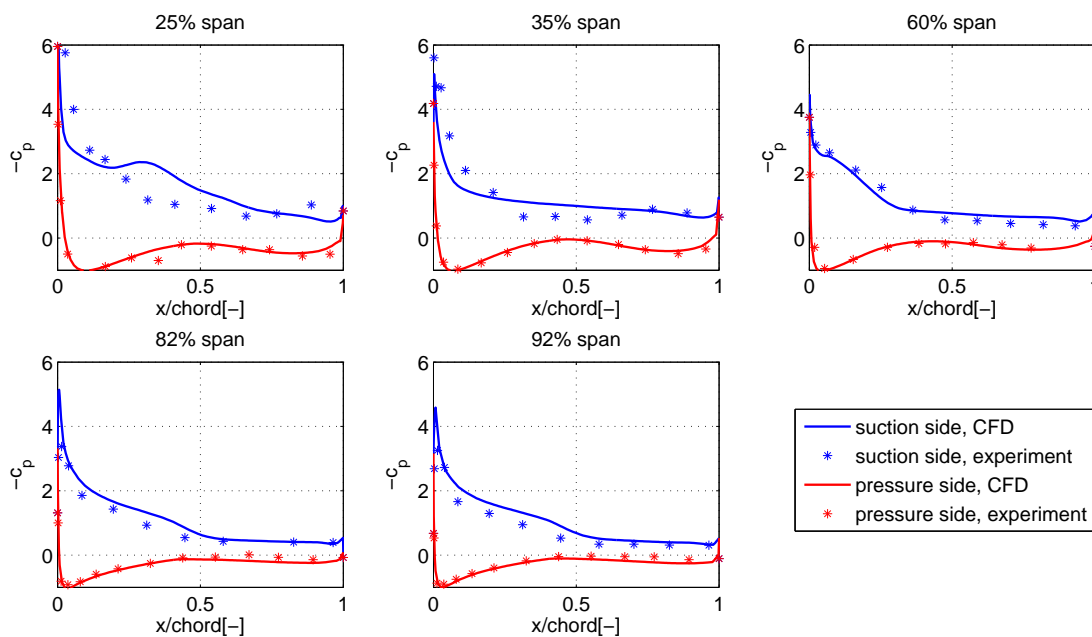

Figure 3.1: Comparison of the predicted pressure coefficient with experiments at different spanwise positions for $\lambda = 4.17$

The torque, T, produced by the rotor is evaluated for the different computational set-ups and for the tip-speed ratios of $\lambda = 4.17$ and $\lambda = 6.67$ the torque is overestimated by about 12% and 6% respectively for the standard fine mesh. However, for the higher tip speed ratio of $\lambda = 10$ the torque is under-predicted by 25%. Analysis of the data shows that for this case, where the inflow velocity is lower, the calculated point where the load is applied is 8% of the span closer to the hub than for the two cases with the lower tip speed ratio. Comparing with the pressure distribution of Fig. 3.3 it is clear that the
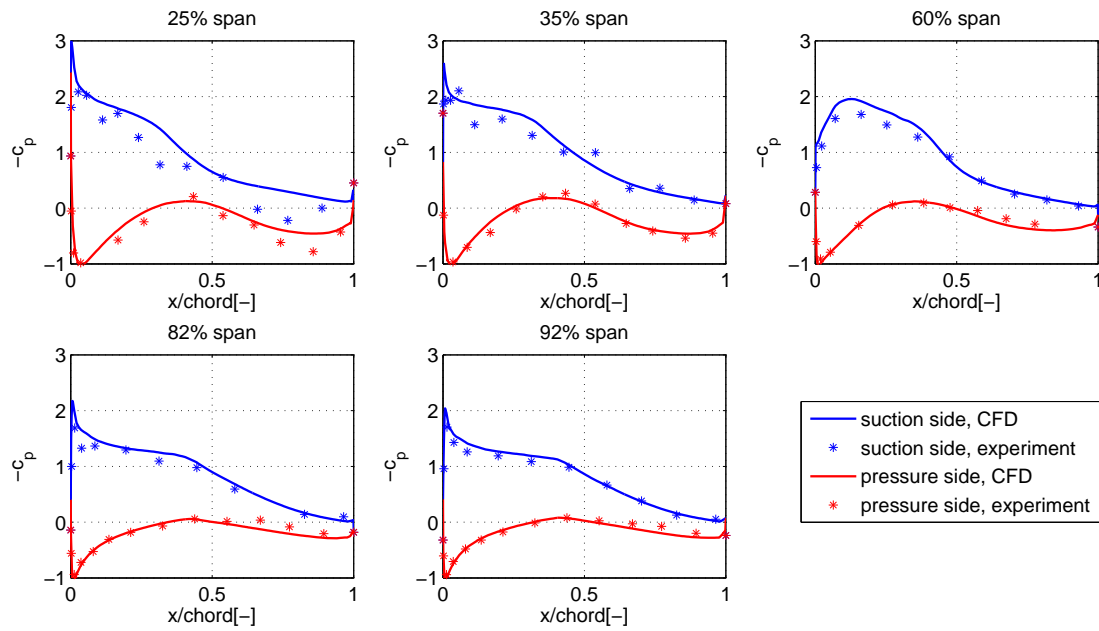
Figure 3.2: Comparison of the predicted pressure coefficient with experiments at different spanwise positions for $\lambda = 6.67$
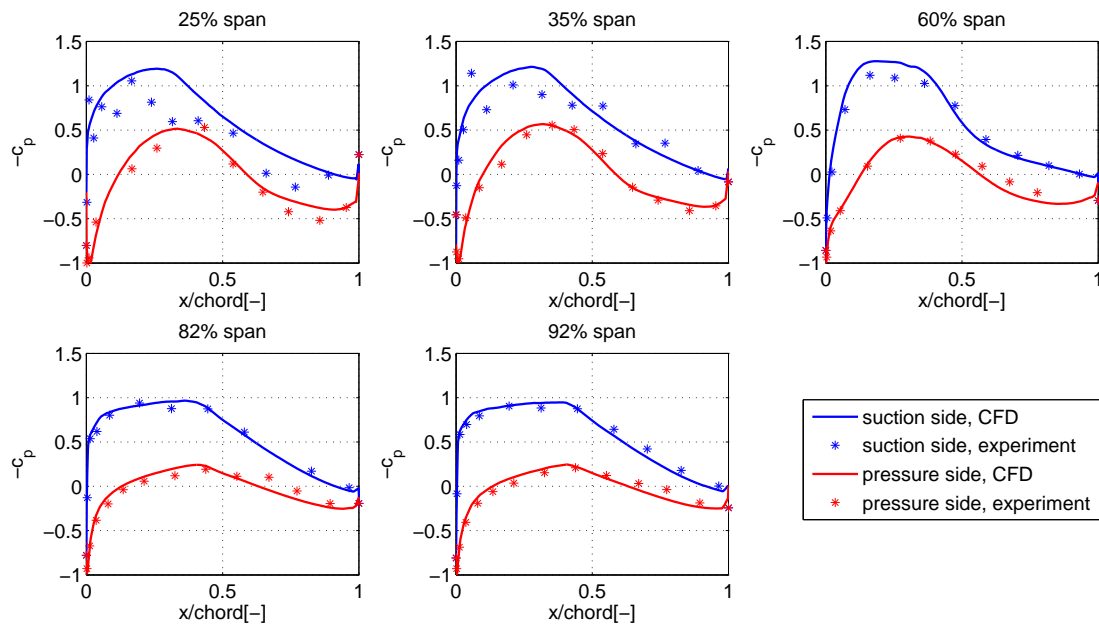

Figure 3.3: Comparison of the predicted pressure coefficient with experiments at different spanwise positions for $\lambda = 10$

blade at 25% span is loaded more than in the experiments, while the values agree for a larger span. This over-prediction of the performance close to the hub results in a shift of the force acting point towards the hub and subsequently a reduction of the simulated torque value.
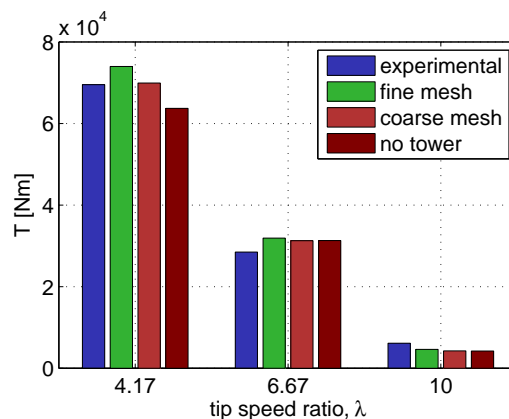

Figure 3.4: Comparison of the estimated torque with experiments, for different tip-speed ratios.

	$\lambda = 4.17$		$\lambda = 6.67$		$\lambda = 10$	
	value [Nm]	diff	value [Nm]	diff	value [Nm]	diff
experimental	695	-	284	-	61.1	-
standard, fine	739.6	6%	319	12%	46.1	-25%
standard, coarse	699.3	0.6%	312.5	10%	42.6	-30%
no tower	637.04	-8%	313	10%	42.1	-31%
rot. cylinder	-	-	320	12%	-	-

Table 3.2: Difference of the calculated torque from experimental values for the different used computational set-ups.

In the MEXICO experiment the thrust was measured by a force measuring balance on the root of the wind turbine model, so the measured axial force includes drag forces acting in the axial direction on all components of the wind turbine. A correction was made to these values by roughly estimating the tower's drag by Bechmann et al.[5]. Both these corrected values as well as the values including the tower drag are used here for comparison with the simulated thrust 3.4. Results show that the corrected values do not correspond as well to the experiments as the values computed for the complete turbine and directly compared to the measured thrust. The correction assumes a drag force of 1010, 390 and 174 N for $\lambda = 4.17$, 6.67 and 10 respectively. However, the present simulations predict a much smaller drag force acting on the tower, which is estimated as 554, 226 and 109 N for the same tip-speed ratios.

	$\lambda = 4.17$		$\lambda = 6.67$		$\lambda = 10$	
	value [N]	diff	value [Nm]	diff	value [Nm]	diff
experimental	2305	-	1661	-	932	-
standard, fine	2732.7	18%	1910.3	15%	1024.5	10%
standard, coarse	2680.6	16%	1900.5	14%	1024.6	10%
no tower	2647.3	-15%	1915.8	15%	1027.5	10%
rot. cylinder	-	-	1917.8	15%	-	-

Table 3.3: Difference between the predicted thrust for the different used computational set-ups and experimental values corrected by [5].

	$\lambda = 4.17$		$\lambda = 6.67$		$\lambda = 10$	
	value [N]	diff	value [Nm]	diff	value [Nm]	diff
experimental	3315	-	2051	-	1106	-
standard, fine	3286	-0.8%	2136	4%	1133	2%
standard, coarse	2680.6	-0.9%	1900.5	6%	1024.6	2%

Table 3.4: Difference between the predicted axial force on rotor, tower and nacelle and experimental values as measured.
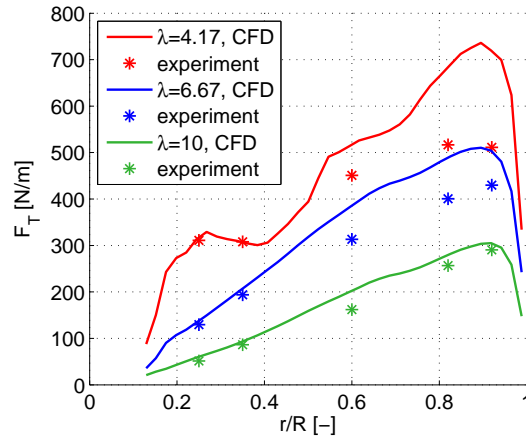

Figure 3.5: Comparison of the predicted spanwise thrust distribution with experimental values for $\lambda = 4.17$, $\lambda = 6.67$, $\lambda = 10$

The thrust coefficient, C_T, is calculated for the three examined tip speed ratios as

$$c_T = \frac{F_x}{\frac{1}{2}\rho u_{ref}^2 A}$$

where F_x is the axial force along the blade, [N], and A the rotor swept area m^2. All other values are as used in Eq. 3.1. It is estimated using the computed thrust on the rotor, as 0.49, 0.87 and 1.05 for tip-speed ratios $\lambda = 4.17, 6.67$ and 10. The lowest thrust coefficient is observed for $\lambda = 4.17$, as only a small fraction of the power available in the

wind at the high speed of $24\,\mathrm{m/s}$ is extracted by the rotor.

Separation occurs on the trailing edge of the suction side at $\lambda = 4.17$ along the complete span of the blade (Fig. 3.6). At the design point and for a higher tip speed ratio the flow remains attached (Fig. 3.6, 3.7). The separation region is larger close to the hub, with the incidence angle at the 35% spanwise position being 24° (Fig. 3.6a). This results in lower aerodynamic efficiency of the rotor at the low tip-speed ratio. According to the momentum conservation law and the Betz theory derived from it, the power extracted by a wind turbine is proportional to the thrust force acting on the rotor (Section 1.2). Therefore, an irregular distribution of the thrust force is observed along the span when separation occurs (Fig. 3.5) and the thrust coefficient for $\lambda = 4.17$ is on average 40% lower than at the design point. Furthermore, the separation introduces additional turbulence in the flow, increasing the turbulence intensity, TI, which is defined as

$$TI = \sqrt{\frac{2/3k}{u_{ref}}} \tag{3.2}$$

where k is the turbulence kinetic energy. This can be seen in the fact that the turbulence intensity directly downstream of the rotor $(0.1\,\mathrm{D})$ is about one order of magnitude larger for $\lambda = 4.17$ than at the operating point(Fig. 3.8).

(a)   (b)   (c)
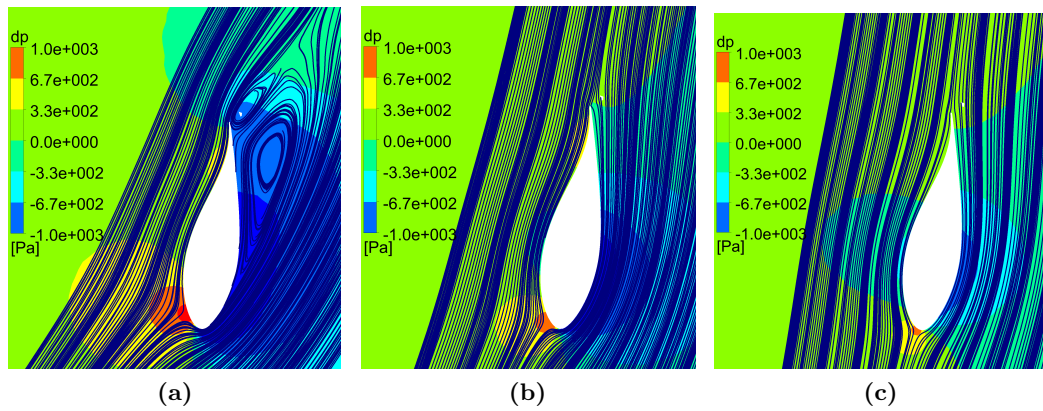
Figure 3.6: Streamlines at 35% span for $\lambda = 4.17$ (a) , 6.67 (b) and 10 (c).

3.1.2   Near Wake

Induced Velocity

The induced velocity across the rotor is evaluated along axial and radial traverses and compared with experimental values. The values for the axial traverses are obtained from sampling along two lines on the XZ plane, which cross the rotor at two different radial positions, at $r_{in} = 0.306\,\mathrm{D}$ and $r_{out} = 0.417\,\mathrm{D}$. The lines span from $1\,\mathrm{D}$ upstream of the
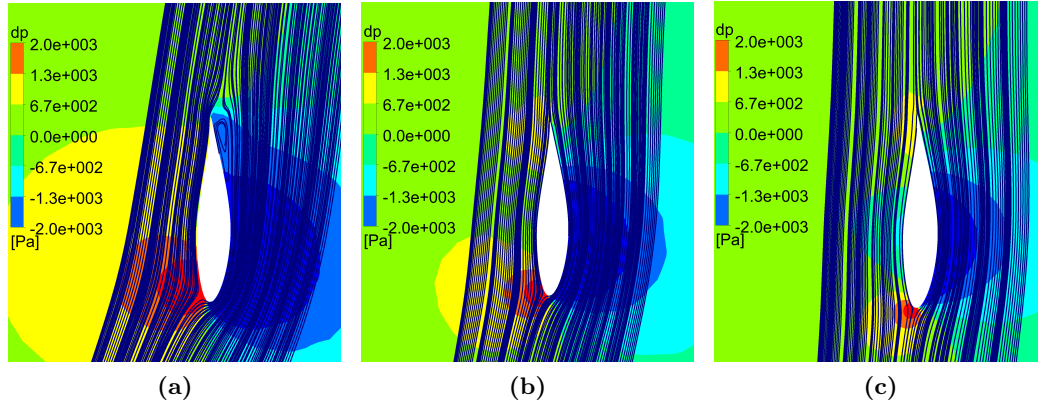
Figure 3.7: Streamlines at 82% span for $\lambda = 4.17$ (a) , 6.67 (b) and 10 (c).
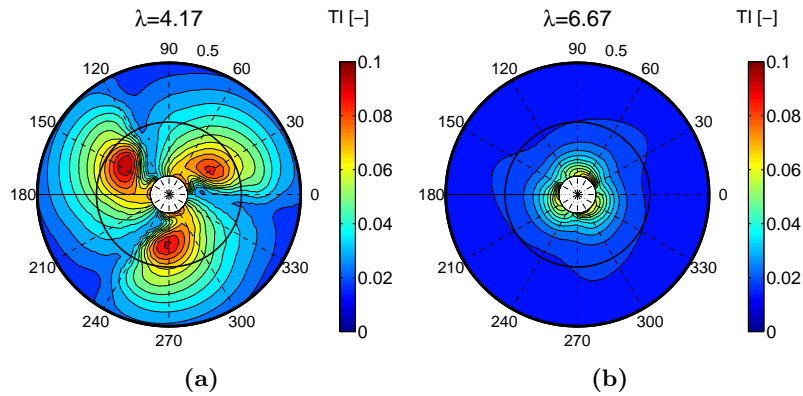

Figure 3.8: Distribution of the turbulence intensity directly downstream of the rotor plane (0.1 D) for $\lambda = 4.17$, (a), and $\lambda = 6.67$, (b).

rotor to 1.3 D downstream (Fig. 3.9a). For the radial traverses the velocity is sampled right upstream and downstream of the rotor plane ($x/D = 0.05$) at seven radial positions with a spacing of 20° (Fig. 3.9b).

The results show good agreement with experimental values (Table 3.5). The difference in the accuracy of the results between coarse and fine mesh for the standard setup is on average only 0.1% of the freestream velocity, showing independence of the results from the grid used. However, the frozen rotor interface used between the rotating and stationary domains, and described in section 2.2.1, appears to have an effect on the results. Namely, the velocity oscillations which are visible in Fig. 3.12 for the case where the tower is omitted and the interface is placed at a distance of 2 D from the rotor plane, are not visible in Figs. 3.10 and 3.11. The velocity oscillations are due to the tip vortices, which break down into a vortex sheet directly at the interface, which is placed at 0.33 D in the standard setup.
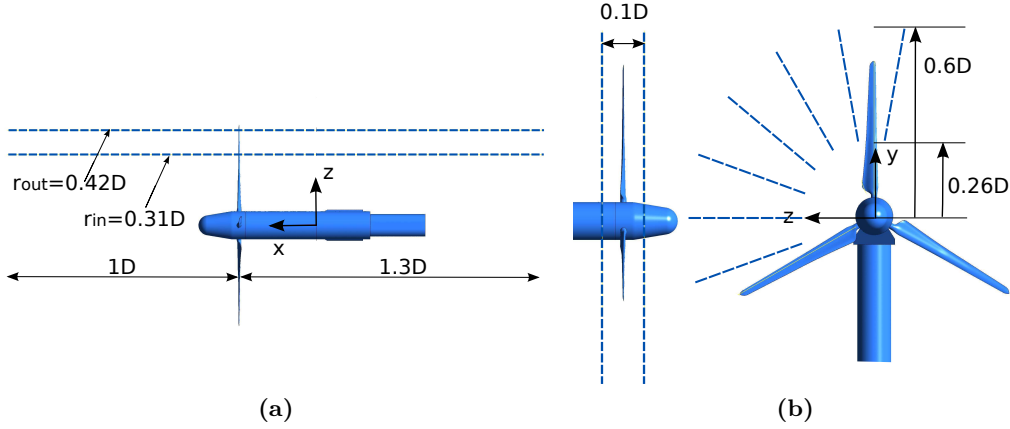
Figure 3.9: Position for the evaluation of the induced velocity along axial traverses (a) and radial traverses (b).

setup and mesh	$\lambda = 4.17$	$\lambda = 6.67$	$\lambda = 10$
standard, fine	3.4%	4.3%	3.7%
standard, coarse	3.1%	4.3%	3.6%
no tower	3.1%	4.2%	3.2%
rot. cylinder	-	4.3%	-

Table 3.5: Difference of the predicted induced velocity from experimental values as percentage of the freestream velocity, u_{ref}, for the different computational set-ups. Measurements along axial traverses and averaged for u, v, w.

The velocities at the radial traverses are also well-predicted for $\lambda = 6.67$, with an average difference of 2.4% and 5.8% of u_{ref} from the upstream and downstream experimental measurements respectively (Fig. 3.13). The maximum difference of 9.6% is found at the 80° traverse. The calculations at the off-design tip speed ratios $\lambda = 4.17$ and $\lambda = 10$ also correspond well to the experimental values with an average difference of 3.5% and 4.6% respectively. The difference between the different set-ups and meshes is negligible, in the order of 0.5%. The average velocity at the rotor plane can be evaluated from these values as the mean between the velocity at the radial traverses shortly upstream and downstream of the rotor plane. The axial velocity at the rotor can subsequently be used to estimate the axial induction factor. The results are summarized on Table (3.6).

Centerline Velocity Deficit

Several wake models use the centerline velocity deficit to estimate the wake width evolution downstream of the rotor [18], [14]. It is therefore useful to have some knowledge about the velocity along the centerline of the wind turbine rotor. In Fig. 3.14 the centerline velocity is plotted against downstream distance, with the evaluation starting at
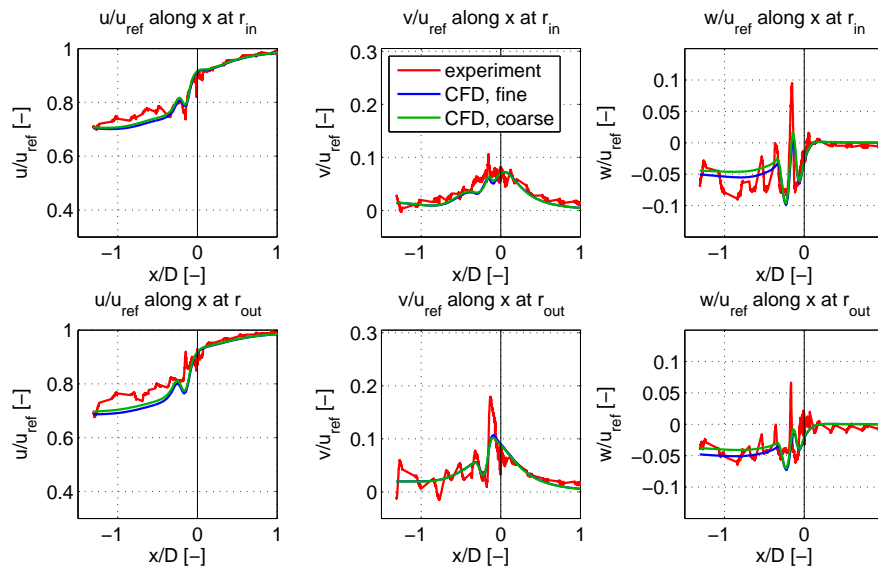
Figure 3.10: Comparison of the predicted velocity components with experiments along two axial traverses for $\lambda = 4.17$
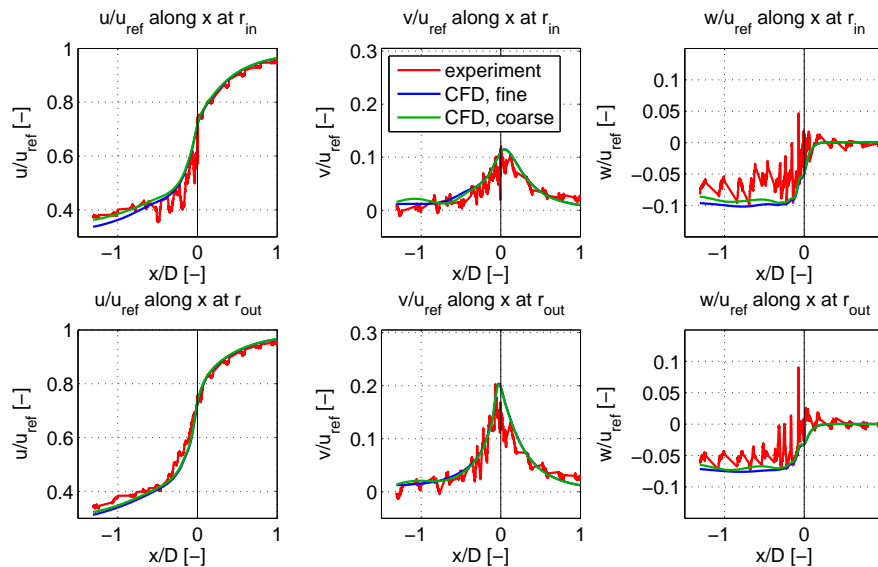

Figure 3.11: Comparison of the predicted velocity components with experiments along two axial traverses for $\lambda = 6.67$

$0.8\,\mathrm{D}$ and $0.5\,\mathrm{D}$ for the case with and without the tower respectively. The reason for this difference is that the non-rotationally symmetric last part of the nacelle is omitted in the setup which does not include the tower.

A comparison between Fig. 3.14a and Fig. 3.14b can show the impact of the tower
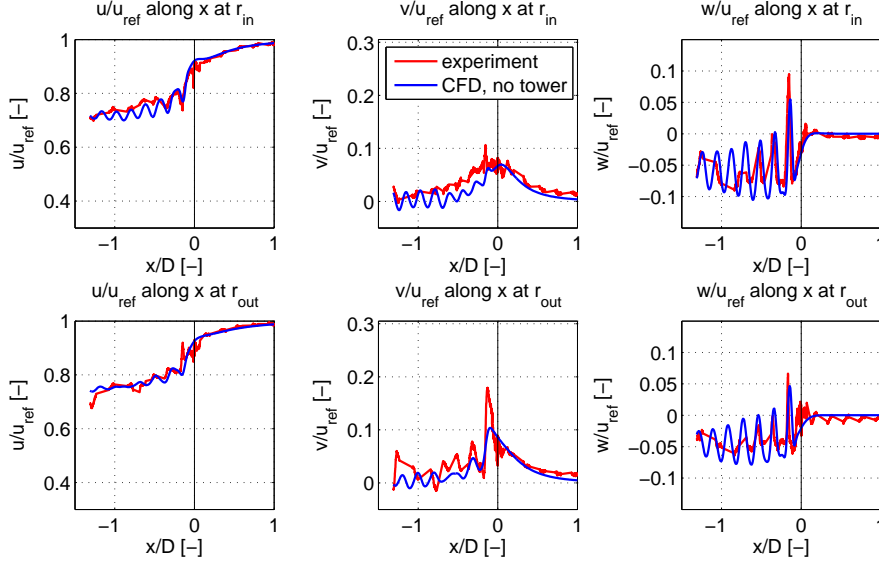
Figure 3.12: Comparison of the predicted velocity components with experiments along two axial traverses for $\lambda = 4.17$ and in the setup where the tower is not included and the domain interface is placed at $9\,\mathrm{D}$ downstream of the rotor plane.

	$\lambda = 4.17$		$\lambda = 6.67$		$\lambda = 10$	
	μ	σ	μ	σ	μ	σ
u_{axial}/u_{ref}	90.9%	2.75%	75.7%	2.54%	56.8%	2.25%
axial induction, a	0.1	-	0.24	-	0.43	-
$C_{p,Betz}$	30%	-	55.7%	-	55.6%	-

Table 3.6: Estimation of the axial velocity by averaging the axial velocity at the radial traverses. Mean value of the velocity at the radial traverses μ, and standard deviation, σ, for $\lambda = 4.17$ and $\lambda = 6.67$, with tower. The axial induction factor, a, and c_P are estimated.

on the velocity deficit. One effect of the tower's presence is that the velocity doesn't increase monotonically, as in Fig. 3.14b. This is due to the disturbance of the flow by the tower's vortex shedding and the non-uniformity introduced by a body that disrupts the symmetry of the wake. Furthermore, while in Fig. 3.14a the separation region at the edge of the nacelle is the same for all three tip speed ratios, a larger velocity deficit is found for $\lambda = 6.67$ and 10, in the case where no tower is included. A possible reason is that the tower is positioned very close to the end of the nacelle and the added turbulence in this region results in a faster recovery. When the tower is omitted the turbulence intensity in this region is lower.

Moreover, the centerline velocity deficit for $\lambda = 6.67$ is larger by 15% u_{ref} when the tower is included. The tower has the least influence on the centerline velocity deficit for $\lambda = 4.17$, where the deficit increases by 8% when the tower is included. Figure
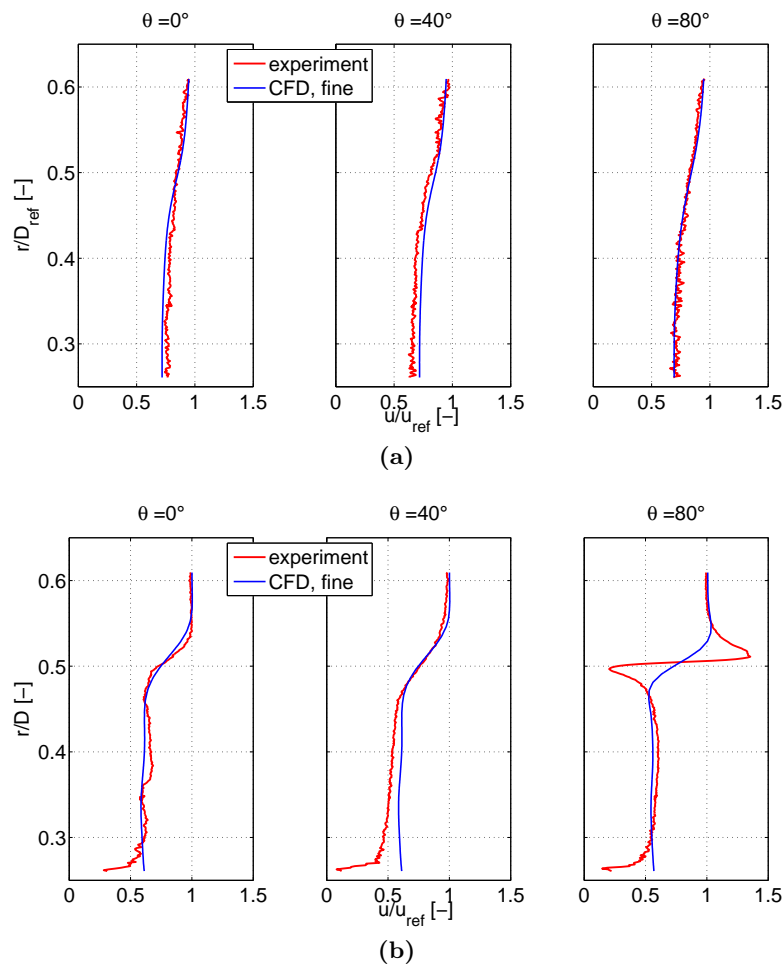
Figure 3.13: Comparison of the predicted velocity components with experimental values along radial traverses upstream $0.05\,\mathrm{D}$ upstream of the rotor, (a), and $0.05\,\mathrm{D}$ downstream, (b), for $\lambda = 4.17$.

3.15 shows the turbulence added in the flow by the tower at a downstream distance of $1\,\mathrm{D}$. The increased turbulence and its interaction with the rotor wake results in a non-symmetric turbulence distribution in the wake, which persists even at $2\,\mathrm{D}$ downstream (Fig. 3.16). When the tower is not included the turbulence distribution is symmetric on a plane parallel to the rotor (Fig. 3.15c, 3.15c).

Wake width

The wake width is a significant wake parameter, as it defines the extent of the region with reduced momentum and increased turbulence, from which less power can be extracted than from the freestream. Moreover, when near wake profiles are used as boundary con-
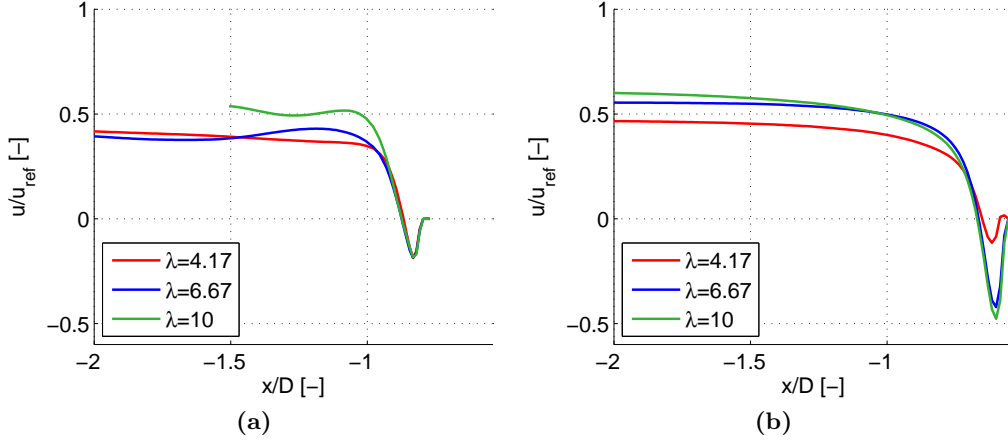
Figure 3.14: Velocity downstream of the rotor for different tip speed ratios and the cases with, (a), and without the tower (b).
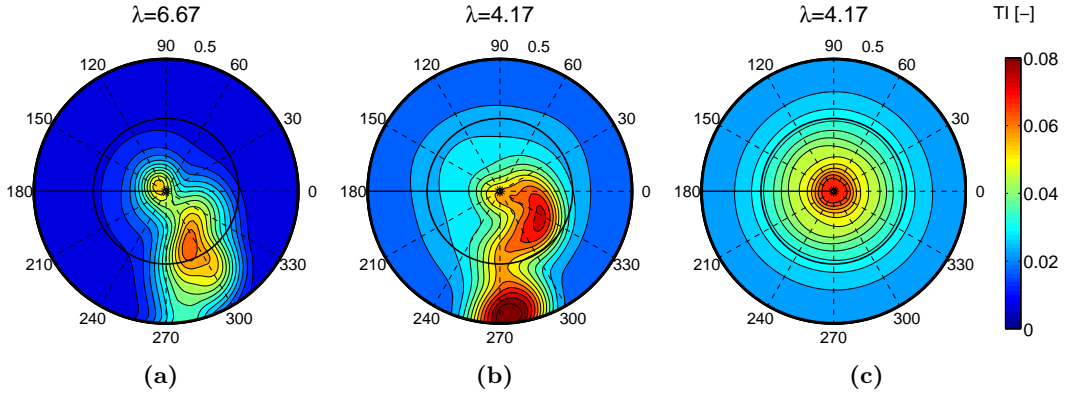

Figure 3.15: Turbulence intensity at $1\,\mathrm{D}$ downstream, in a plane of r=0.5[D] with the tower at $\lambda = 6.67$ (a), and $\lambda = 4.17$ (b) and without the tower at $\lambda = 4.17$ (c).

ditions for the calculation of the far wake, the shape and range of the wake region should be well-defined. The near wake region is here examined until $2\,\mathrm{D}$ downstream.

Due to the pressure increase directly upstream of the rotor, which causes the streamlines to diverge, and due to the mixing of the wake with freestream, the wake expands with downstream distance (Fig. 3.18). According to Barthelmie et al.[4] the width of a single turbine's wake can be defined as the position where the wind speed ratio u/u_{ref} is between 0.95 and 0.99 . As the exact position where the wind speed amounts to $0.99u_{ref}$ cannot be easily determined by field experiments, the choice for this limit is subjective. However, as the current project applies to CFD simulations, where full knowledge of the wake values is provided, a limit of 99% is chosen for the wake boundary.
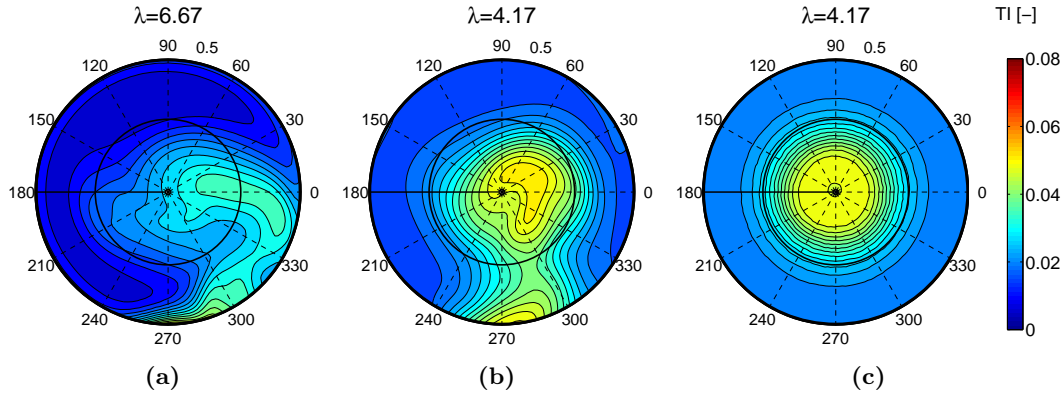
Figure 3.16: Contours of turbulence intensity at $2\,$D downstream, in a plane of r=$0.5\,$D, with the tower at $\lambda = 6.67$ (a), and $\lambda = 4.17$ (b) and without the tower at $\lambda = 4.17$ (c).

The contours of the axial velocity deficit on the XY plane is shown in Fig. 3.18 for the three different tip speed ratios, and the non-uniformity caused by the tower is clearly visible. Due to the presence of the tower and the additional mixing that it causes, the velocity deficit in the lower part of the wake in the XY plane ($Y < 0$) is smaller by 7%, 3% and 9% u_{ref} for $\lambda = 4.17, 6.67, 10$ respectively. However, a more irregular flow with larger in-plane components and additional turbulence is expected. In addition, the wake is skewed in the XZ plane for higher tip speed ratios (Fig. 3.19), a behavior which is not observed when the tower is not included. This effect can be attributed to the interference of the rotating wake and tip vortices with the tower and the tower-generated vorticity, as the vorticity strength and tangential velocity of the wake both increase with a decreasing tip-speed ratio. For the simulations without the tower the distribution of the axial, radial and tangential velocities in the wake is axisymmetric (Fig. 3.20). This fact is also clear in the comparison of Tables 3.7 and 3.8 where the mean values differ by about 5% on average but the values for the standard deviation are significantly larger when the tower is included.

The largest expansion is observed for the highest tip speed ratio, $\lambda = 10$, where the wake width at $2\,$D reaches 162% of the rotor diameter. Very little expansion is observed at the highest wind speed, for $\lambda = 4.17$, where the width amounts to $114\%\,$D and at the operating point the width is $134\%\,$D (Fig. 3.17a). Oscillations seen in the wake radius for $\lambda = 4.17$ are due to the presence of distinct tip vortices at this tip speed ratio, which result in a local decrease in velocity. The increase of the wake radius with downstream distance can be well approximated by second order polynomials with a relative error of on average 5%. A larger error is inroduced by $\lambda = 4.17$, due to the frequent oscillations. The wake expansion for different tip-speed ratios corresponds to the expected behavior, as experiments in controlled environments have shown the same effect for a tip-speed ratio variation [27]. Finally, relating the wake width at $2\,$D to the thrust coefficient for the different tip speed ratios examined, the wake's width increases with C_T (Fig.
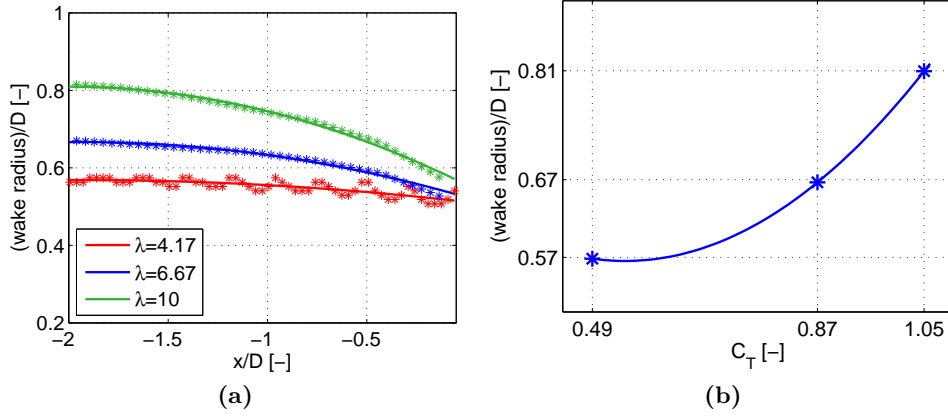
3.17b).

Figure 3.17: Wake extension for different tip-speed ratios (a) and correlation of wake width to thrust coefficient (b)
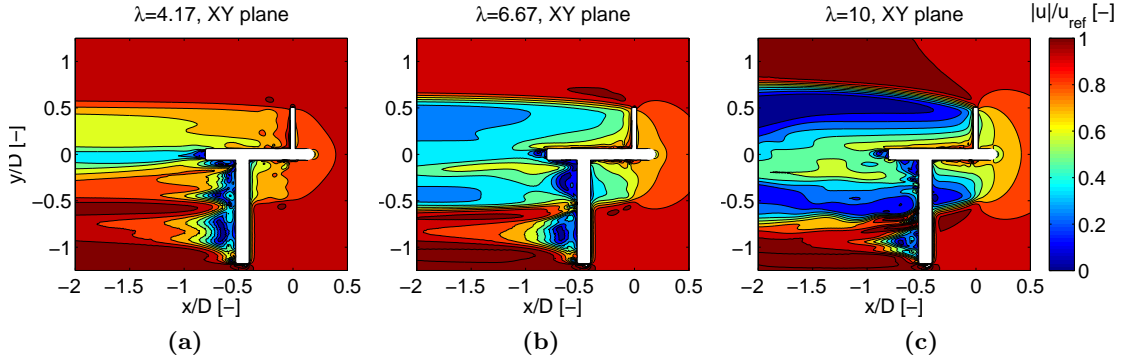

Figure 3.18: Contours of total velocity in the XY plane for $\lambda = 4.17$, $\lambda = 6.67$, $\lambda = 10$.

Concerning the large expansion at $\lambda = 10$, according to Whale et al. the near wake at tip speed ratios as high as 10 acts as a solid rotating impeding in the free stream. This introduces blockage, which results in a large wake expansion as the flow must diverge around the wake region [29]. This occurs when the turbine is operating in the so-called turbulent wake state, defined by Eggleston and Stoddard when $C_T > 1$. Indeed, for $\lambda = 10$ a thrust coefficient of $C_T = 1.05$ is estimated. Furthermore, a wake expansion and subsequent contraction is observed beyond 3 D, which is also captured in the present simulations (Fig. 3.20c). As, however, the mesh quality decreases after 2 D, a finer mesh should be used to examine this complex behavior with higher accuracy.

The velocity profiles at different downstream distances also help to understand the characteristics of the wake. At a downstream distance of 2.25 D the velocity deficit is compared with the deficit estimated by the ECN Wakefarm model [3]. The ECN
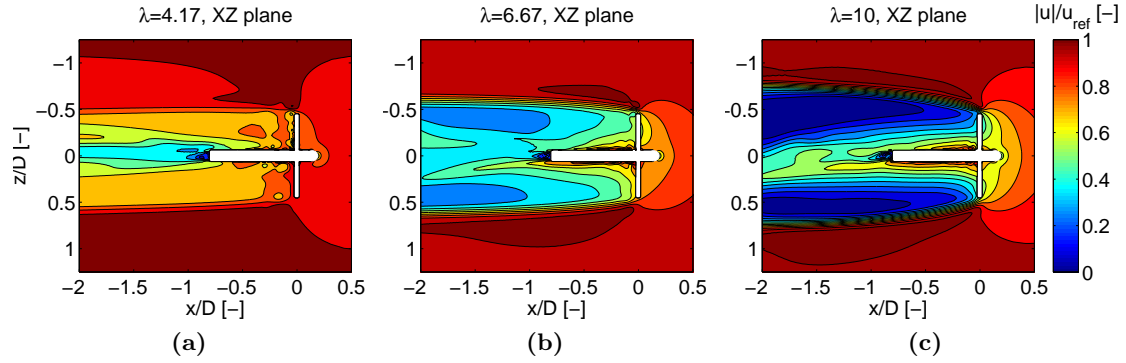
Figure 3.19: Contours of total velocity in the XZ plane for $\lambda = 4.17$, $\lambda = 6.67$, $\lambda = 10$.
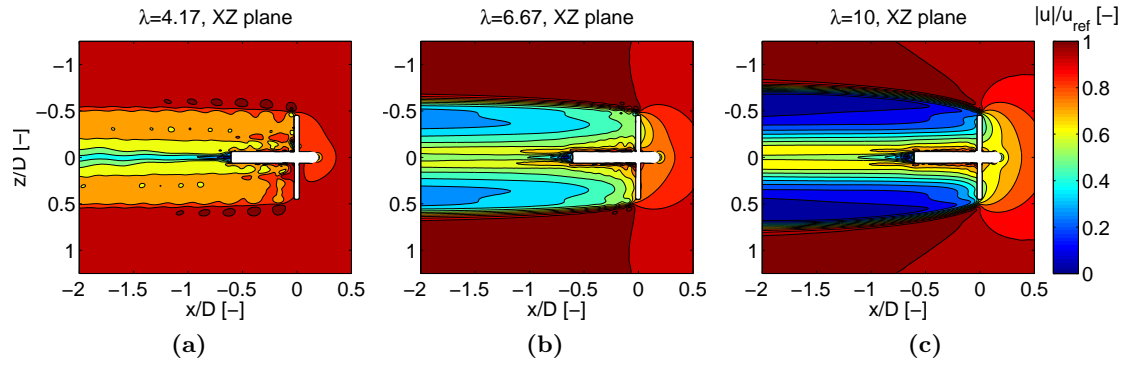

Figure 3.20: Contours of total velocity in the XZ plane for $\lambda = 4.17$, $\lambda = 6.67$, $\lambda = 10$ in the setup without the tower.

Wakefarm model assumes a velocity deficit profile of a Gaussian form estimated by the function

$$u_{def} = 1.3(1 - \sqrt{1 - c_T})u_{ref} \cdot e^{-0.5\left(\frac{z}{r\sigma_y}\right)^2} \tag{3.3}$$

where u_{def} is the velocity deficit, c_T the thrust coefficient, z the lateral position in the wake, r the rotor radius and σ_y a factor for the wake width, which is calculated as $\sigma_y = D\sqrt{(1-a)/(1-2a)}$ where a is the axial induction factor and D the rotor diameter. The model assumes a maximum velocity deficit along the centeline. However, according to the present simulations this is the case only for $\lambda = 4.17$, where less than the optimal power is extracted by the outer half of the blade. At the operating point, $\lambda = 6.67$, the maximum velocity deficit is found at the outer part of the blade rather than at the center of the rotor plane (Fig. 3.22). Furthermore, the velocity deficit is not axisymmetric when the tower is included, as can be seen by comparing Fig. 3.19 and Fig. 3.20. It should, however, be noted that in the present model's geometry the length and diameter of the nacelle are larger relative to the rotor diameter in comparison to real wind turbines. Namely the nacelle has a diameter of $0.1\,D$ and a length of $0.8\,D$, whereas

these dimensions would amount to $0.05\,\mathrm{D}$ and a length of $0.15\,\mathrm{D}$ for a commercial $3\,\mathrm{MW}$ turbine. The tower's diameter is $0.1\,\mathrm{D}$, against $0.05\,\mathrm{D}$ for commercial turbines and it is located farther downstream, which amplifies its signature at $2\,\mathrm{D}$. Nevertheless, the large discrepancy in wake width between CFD simulations and the model cannot be attributed to geometry differences and a velocity deficit profile at the end of near wake model should account for this difference.

(a)   (b)
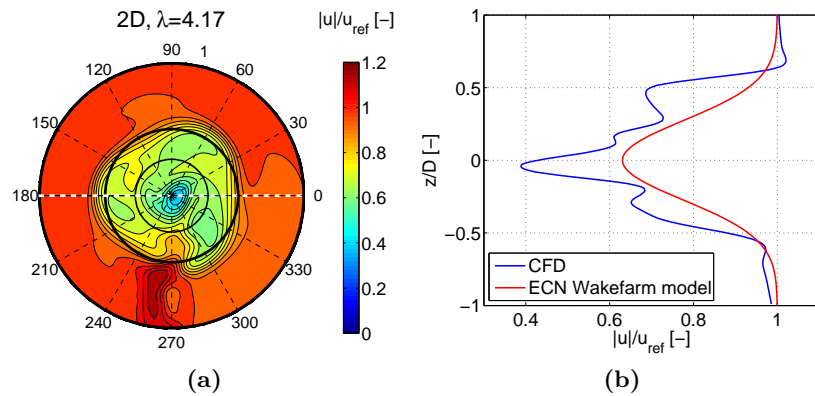
Figure 3.21: Contour of velocity deficit at $2\,\mathrm{D}$, in a plane of r=1[D] for $\lambda = 4.17$ (a) and comparison of deficit profile to Gaussian profile used in ECN Wakefarm model.

(a)   (b)
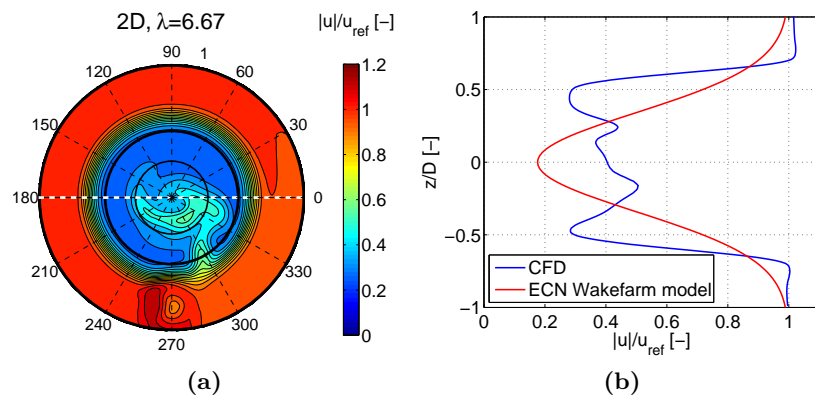
Figure 3.22: Velocity deficit at $2\,\mathrm{D}$, in a plane of r=1[D] for $\lambda = 6.67$ (a) and comparison of deficit profile to the ECN Wakefarm model.

Flow angles

Downstream of the rotor, the wake rotates with an angular velocity in the opposite direction to that of the rotor to satisfy the conservation of angular momentum. The rotational kinetic energy represents a loss, as it cannot be recovered for useful energy

conversion. At the same time the flow is accelerated radially due to centrifugal forces generated by the rotating plane and due to the wake expansion. This results in in-plane velocity components in the direction of the Y an Z axes. The ratio of these components to the axial velocity introduces pitch and yaw angles in the flow. Therefore, the flow angles indicated here as pitch, θ and yaw, γ, designate the angle between the velocity vector and the axes Y and Z respectively (Fig. 3.23).
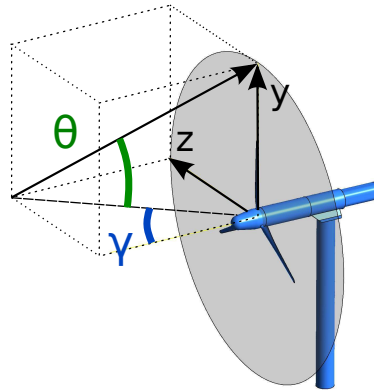

Figure 3.23: Definition of yaw angle, γ and pitch angle, θ.

The magnitude of the pitch and yaw angles illustrates the strength of the in-plane velocity components relative to the axial velocity, helping to visualize the overall wake rotation and vortices. As with the axial velocity, the presence of the tower results in a non-uniform distribution of the flow angles in the wake, and the tower's influence still remains visible until 2 D downstream (Fig. 3.26). Tracking the flow angles at different downstream positions shows the decay of the wake region, as the flow far from the turbine should be dominated by the axial component.

For $\lambda = 6.67$, the angles are distributed over the whole swept area of the rotor, whereas they are much more concentrated at the inner part of the plane ($r < 0.25$ D) for $\lambda = 4.17$, due to the smaller wake width. Furthermore, the magnitude of the angles is reduced with downstream distance but they are distributed over a larger region due to the beginning of the mixing of the slow wake with the freestream flow (Fig. 3.24). Moreover, the influence of the tip vortices on the flow is clearly visible in the periodic increase and decrease of the pitch angles in Fig. 3.25, where the tower is omitted. The yaw angles exhibit a similar behavior as the pitch angles as seen on Table 3.7.

The mean in-plane velocity magnitudes and angles at 2 D downstream are summarized on Tables 3.7 and 3.8 for the cases with and without the tower respectively. The mean tangential velocity is, as expected, larger at 1 D, as is the magnitude of the yaw and pitch angles. This is the case because as the streamtube expands the relation $\omega_1 r_1 = \omega_2 r_2$ must hold, so the tangential velocity must decrease. Additionally, dissipation of the rotational kinetic energy in turbulence occurs as the wake is mixing with the freestream flow. The non-uniformity due to the tower is clearly visible by comparing Fig. 3.27a

and Fig. 3.26d with the other plots of Fig. 3.26 and also by comparing the standard deviations of the values, which are larger when the tower is included (Tables 3.7, 3.8). The vector plots show the distribution of the in-plane velocities in a plane of radius $r = 0.5\,\mathrm{D}$. However, within the range $r < 0.5\,\mathrm{D}$ the radial component is in all cases at least one order of magnitude smaller than the tangential component, so the tangential velocity dominates in the plane. For $r > 0.5\,\mathrm{D}$ the radial components are larger than the tangential, as the wake expands beyond the rotor radius. By a downstream distance of $2\,\mathrm{D}$ the radial components decay to nearly zero for both tip-speed ratios.
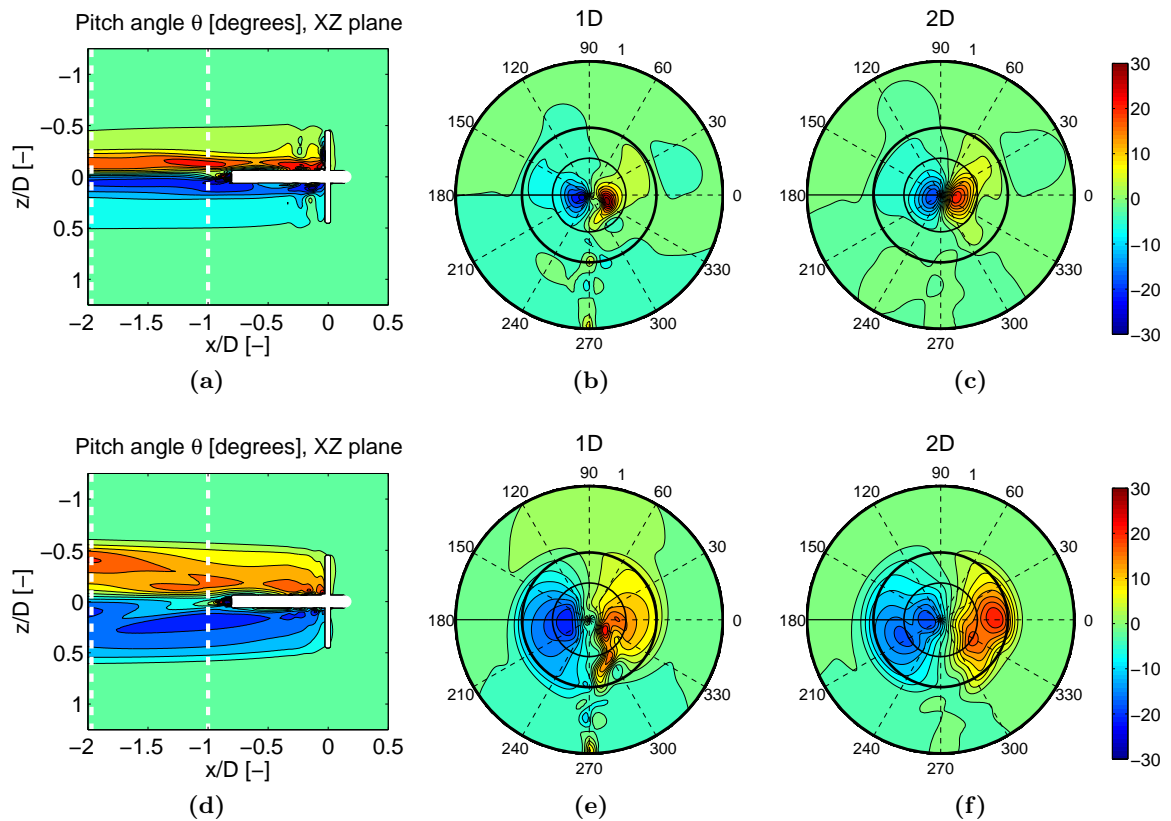
Figure 3.24: Pitch angles in the XZ plane, and section planes of radius $r = 1\,\mathrm{D}$ at $1\,\mathrm{D}$ and $2\,\mathrm{D}$ downstream distance for $\lambda = 4.17$ (a), (b), (c) and $\lambda = 6.67$ (d), (e), (f).

The tangential velocity u_{tan} is a measure for the strength of the wake rotation, which occurs due to the conservation of angular momentum. Averaged over the rotor area at $1\,\mathrm{D}$ downstream, u_{tan} is approximately 9% u_{ref}, and it is about 1% lower at $2\,\mathrm{D}$ than at $1\,\mathrm{D}$. While the tangential velocities for $\lambda = 4.17$ are on average similar to $\lambda = 6.67$, the maximum for $\lambda = 4.17$ is 8% u_{ref} higher, and the region of high u_{tan} is smaller and concentrated around the hub, in the region of the hub vortex. Therefore, the wake

Figure 3.25: Pitch angles for $\lambda = 4.17$ (a) and (b), results from isolated rotor simulations.

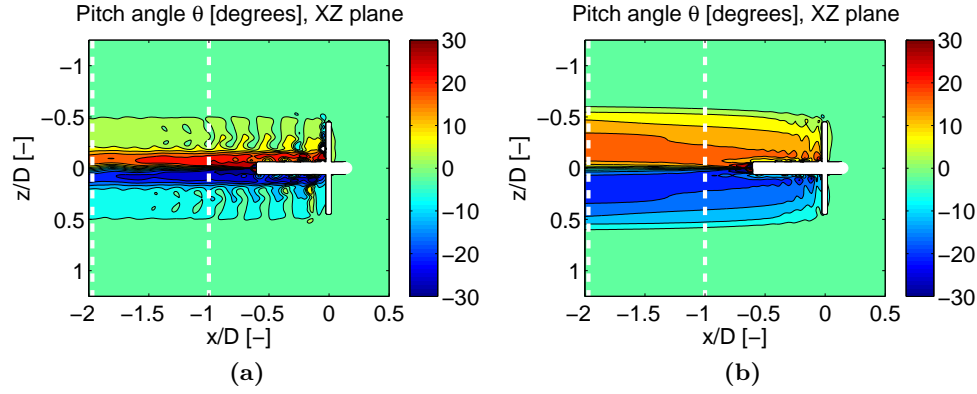|	1D, $\lambda = 4.17$		2D, $\lambda = 4.17$		1D, $\lambda = 6.67$		2D, $\lambda = 6.67$	
	μ	σ	μ	σ	μ	σ	μ	σ
u_{axial}/u_{ref}	64%	6%	64%	5%	40%	5%	36%	5.3%
u_{rad}/u_{ref}	0.1%	3.1%	0.01%	3%	0.46%	2.4%	0.4%	3.5%
u_{tan}/u_{ref}	9.3%	3.3%	8.2%	2.5%	9%	2.25%	8.4%	2.9%
yaw angle [°]	-1.5	7.8	-0.7	5.6	-1.8	9.8	-2.4	10.8
pitch angle [°]	1	6.4	1.1	6.24	0.7	9.5	2.7	9.3

Table 3.7: Mean values, μ, and standard deviations, σ, of the flow properties at 2 D downstream of the turbine for $\lambda = 4.17$ and $\lambda = 6.67$, with tower

	1D, $\lambda = 4.17$		2D, $\lambda = 4.17$		1D, $\lambda = 6.67$		2D, $\lambda = 6.67$	
	μ	σ	μ	σ	μ	σ	μ	σ
u_{axial}/u_{ref}	68%	1%	66%	0.8%	44.9%	0.07%	41%	0.03%
u_{rad}/u_{ref}	0.35%	1.4%	0.12%	0.8%	0.7%	0.12%	0.2%	0.05%
u_{tan}/u_{ref}	10.7%	1.6%	8.7%	0.8%	12.3%	0.08%	11.2%	0.04%
yaw angle [°]	0.01	7.5	-0.17	5.8	-0.06	11	-0.01	11.3
pitch angle [°]	0.005	7.4	0.3	5.8	0.1	11	0.1	11.4

Table 3.8: Mean values, μ, and standard deviations, σ, of the flow properties at 2 D downstream of the turbine for $\lambda = 4.17$ and $\lambda = 6.67$, without tower

rotational speed, ω_2, can be estimated as

$$\omega_2 = \frac{u_{tan,mean}}{(R)} \approx 1.32 \,\text{rad/s} \approx 0.03 \cdot \omega_{rotor} \qquad (3.4)$$

where $u_{tan,mean}$ is the average tangential speed over a downstream positioned plane of radius $0.5D = R$, where R is the rotor radius. Given the values of Table 3.8 this results in a value which is about one fourth of the rotor's speed and an angular induction factor $a_{prime} = 0.015$. Moreover, the three symmetric structures in the contour plot of the

tangential velocity for $r > 0.25\,\mathrm{D}$ and $\lambda = 4.17$ are caused by the tip vortices, which are substantially more distinct at the lower tip-speed ratio (Fig. 3.27). At higher tip speed ratios the vortices break down into a vortex sheet and as a result they are not individually visible in the velocity field.
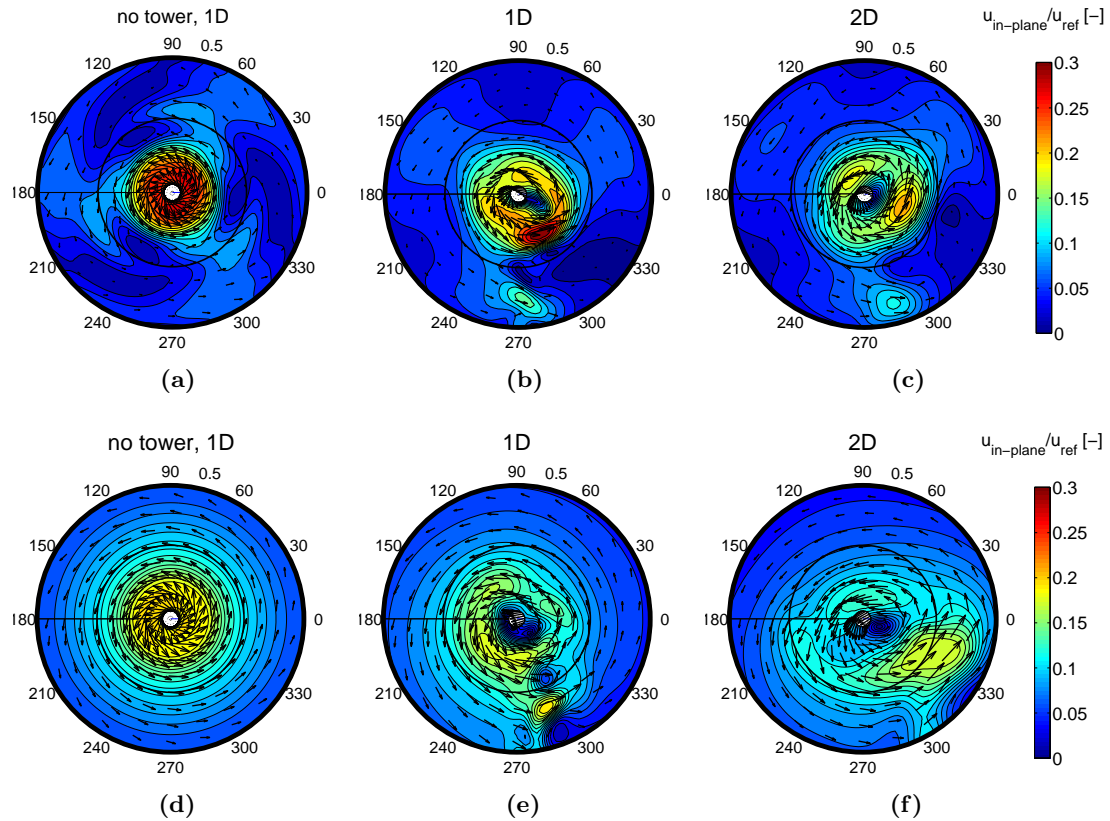

Figure 3.26: In-plane velocity vectors on plane of $r = 0.5\,\mathrm{D}$, superposed on contours of in-plane velocity magnitude for $\lambda = 4.17$ (a), (b), (c) and $\lambda = 6.67$ (d), (e), (f).

Vorticity

According to the Kutta-Jukowski theorem, each section of the rotor blade generates a lift force proportional to the local bound vorticity [13]. As with any lift-generating wing, a horseshoe vortex must be formed at the blade to be in accordance with Helmholtz's second theorem, specifying that "a vortex filament cannot end in fluid but it must extend to the boundaries of the fluid or form a closed path". Knowing the position of the tip vortex cores, a prescribed vortex design can be implemented, resulting in higher accuracy than an actuator disc model. The nondimensional vorticity, ζ_n, is here defined as

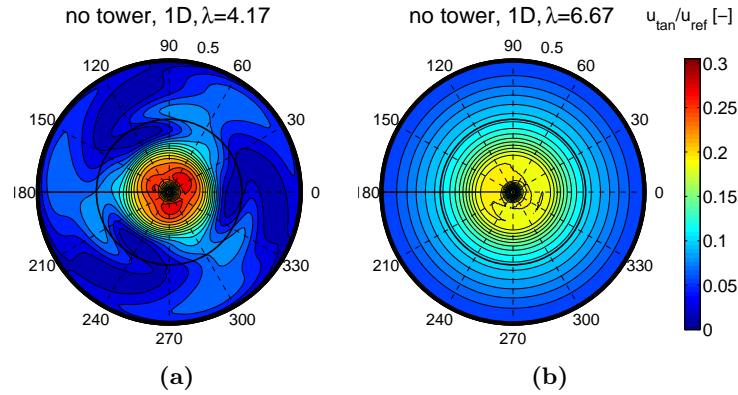$$\zeta_n = \frac{\zeta D}{u_{ref}} \tag{3.5}$$

Figure 3.27: Tangential velocity at $1\,\mathrm{D}$ in a plane of radius $r = 1\,\mathrm{D}$ for $\lambda = 4.17$ and $\lambda = 6.67$ and the setup without the tower.

where ζ is the vorticity in $[s^{-1}]$, D the rotor diameter and u_{ref} the freestream speed. Vorticity is generated both by the blades and by the tower.

As expected, a larger vortex strength is observed as the tip-speed ratio increases, which is also documented by Ebert et al. [12], and Whale et al. [29]. For the low tip-speed ratio $\lambda = 4.17$ the large incidence angle results in reduced lift, which subsequently results in lower bound vorticity on the blade and lower vorticity in the tip and hub vortices (Fig. 3.28). Additionally, the increased turbulence in the wake of the low tip-speed ratio case may result in a quicker dissipation of the vortices. In Fig. 3.28, the logarithm of the non-dimensionalized vorticity is plotted, to help visualize both small and large-scale vortex structured in the same plot.

The higher vorticity around the tower is also more pronounced for the higher tip speed ratio. The Reynolds number for the tower is in this case $Re \approx 2.5 \times 10^5$. At that Reynolds number the frequency of the vortex shedding downstream of a cylinder is directly proportional to the freestream velocity. This is because this frequency, f, is described by the Strouhal number, $St = (f \cdot D_{tower})/u_{ref}$, which at that range of Re is constant. Therefore, with increasing u_{ref} (and decreasing λ) the frequency of the vortex shedding increases, introducing more turbulence and resulting in smaller vortices.

Furthermore, a meaningful parameter used to examine the tip vortices is the so-called vortex pitch, p_v, which describes the axial distance that a vortex is transported during one blade revolution [29]. This is approximated by Wood [31] as

$$p_v \approx \frac{1 + u_2}{2\lambda} \tag{3.6}$$

where u_2 is the average velocity through the blades at the rotor plane. This indicates that at higher tip-speed ratios the vortex cores are closer to each other, and therefore are soon merged into a vortex sheet, as seen on Fig. 3.28. The pitch for $\lambda = 4.17, 6.67$
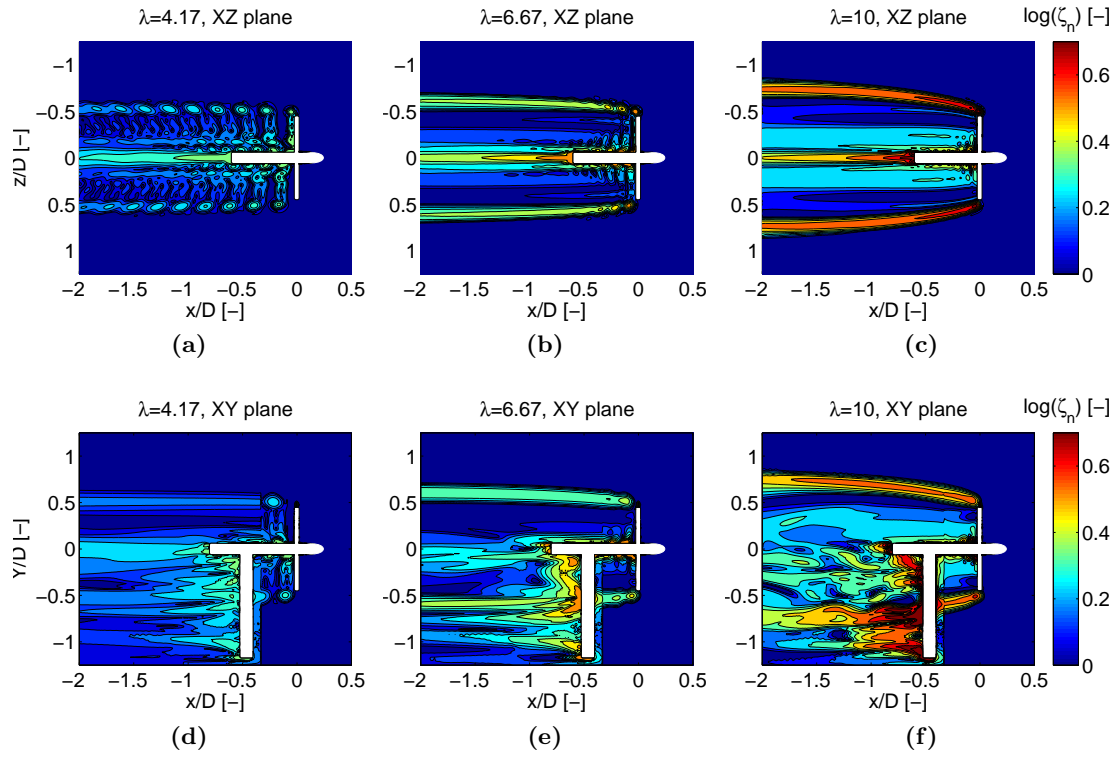
Figure 3.28: Contours of vorticity at different tip-speed ratios as seen in the setup without the tower, (a), (b), (c) and with the tower (d), (e), (f).
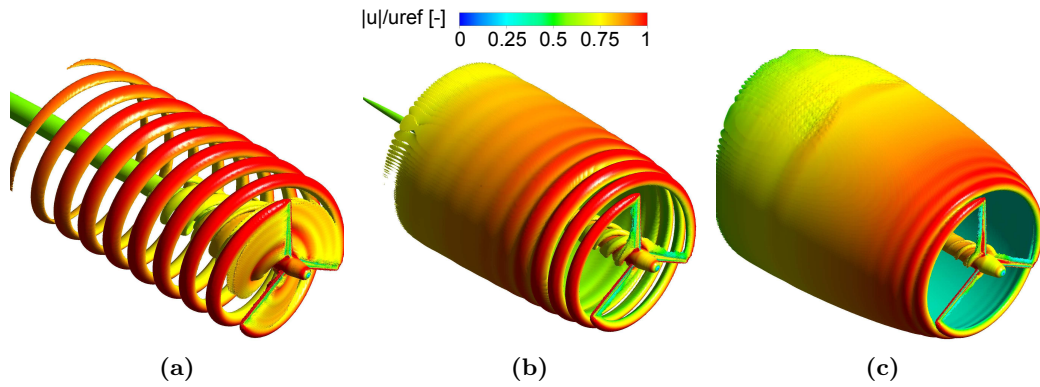
Figure 3.29: Isosurface of constant vorticity, different for each tip-speed ratio $\lambda = 4.17$ (a), $\lambda = 6.67$ (b), $\lambda = 10$ (c). Colored by non-dimensionalized total velocity.

and 10 is estimated to be $p_{v4.17} = 0.67\,\mathrm{D}$ $p_{v6.67} = 0.39\,\mathrm{D}$ $p_{v10} = 0.24\,\mathrm{D}$. The paths of the tip vortices are better visualized in Fig. 3.29

3.1.3   Unsteady Simulations

For the case of $\lambda = 4.17$ an unsteady analysis has been carried out, to clarify whether the steady state results accurately represent the flow field or whether unsteady phenomena significantly affect the flow in the wake. The $\lambda = 4.17$ case is chosen, as the larger separation which occurs at the blades is most likely to introduce unsteady effects.

The simulation and timestep options for the unsteady run are summarized on Table 3.9. The results of the steady-state simulation are used as initial conditions. To certify the convergence of the unsteady simulation, the velocity and pressure are monitored downstream of the rotor. For the three-bladed rotor a periodic change of the flow properties is expected every $120\,^\circ$. This is indeed observed, so convergence can be assumed to be reached (Fig. 3.30).
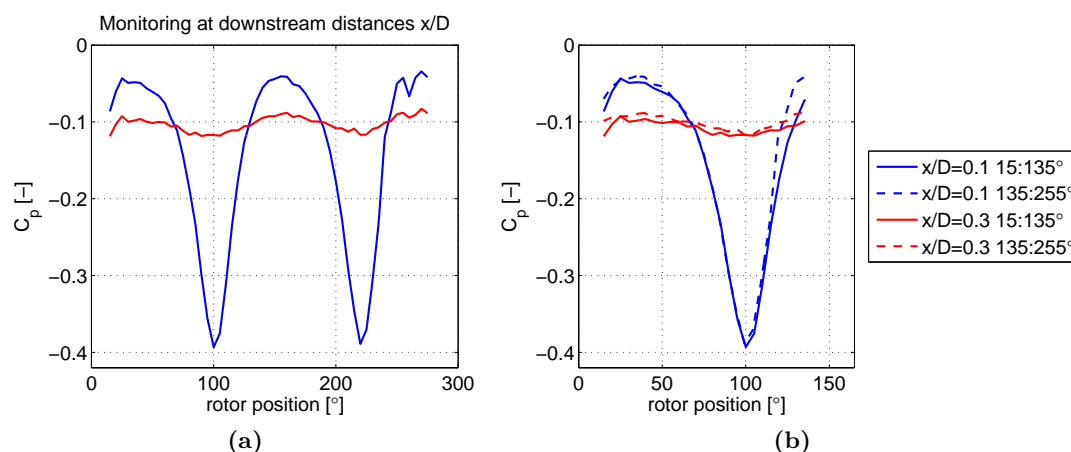
Figure 3.30: Periodic variation of the pressure at two downstream positions (a) and overlap of two subsequent periods (b)

total time [s]	0.1413
time per timestep [s]	9.8×10^{-5}
timesteps per degree of revolution [ts/$^\circ$]	4
coefficient loop iterations	5

Table 3.9: Solver setup for the unsteady simulation.

Comparison of the unsteady results to steady state simulations and experiments along axial traverses show good overall agreement with the steady-state results (Fig. 3.31). The mean difference for all velocity components between unsteady and experiments is $3.5\%\ u_{ref}$, which is the same as for the steady-state results. For the radial traverses the velocity is monitored at the 0° traverse (Fig. 3.32) for different rotor positions. This way the time-accurate velocity deficit upstream and downstream can be derived and compared with steady state and experimental values. The difference between steady

state and unsteady is 2% u_{ref} for the upstream and 3.7% u_{ref} for the downstream
position on average, matching the experimental values with an average error of 2.5%
u_{ref} (Fig. 3.32). A larger error for the downstream position in steady-state results is
justified by the fact that separation occurring at the blades at that tip-speed ratio results
in elevated turbulence intensity and more pronounced unsteady behavior. This region
is therefore captured best by unsteady simulations. Comparing the axial velocity on the
XY and XZ plane in the wake region until 0.75 D downstream results in a difference of
0.8% u_{ref} for the XY and 0.4% u_{ref} for the XZ plane. The larger difference for XY is
caused by the fact that the tower region, where unsteady separation and vortex shedding
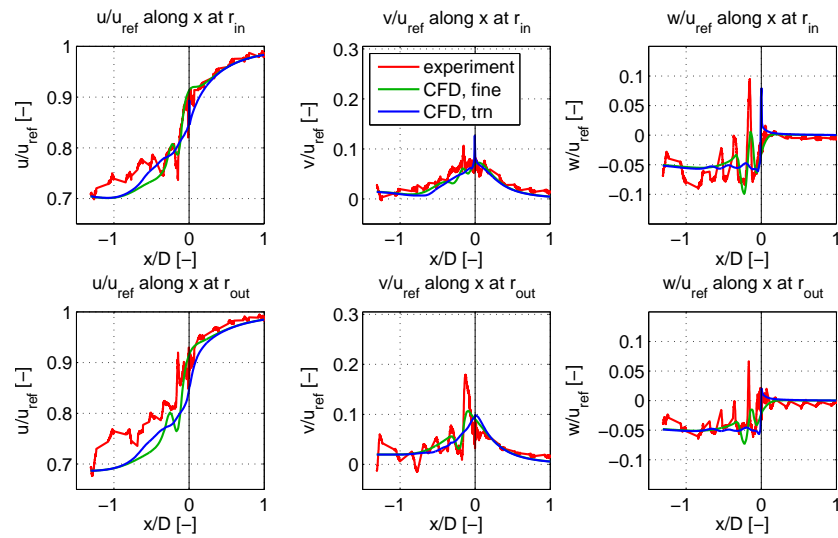occur, is captured in that plane.

Figure 3.31: Comparison of the estimated velocities to steady state simulations and experiments
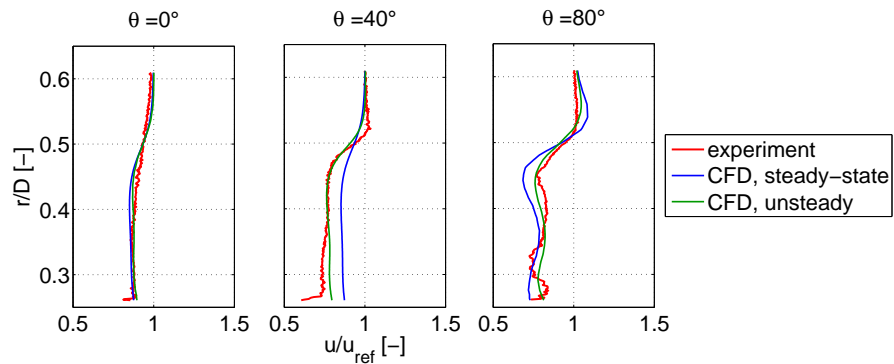along axial traverses .

Figure 3.32: Comparison of the estimated velocities to steady state simulations and experiments
along radial traverses.

The variation of the in-plane velocities at 0.5 D is captured by the unsteady simulation

(Fig. 3.33). Three symmetrical structures of higher in-plane components are clearly
visible in the wake. The structures have the characteristic shape of a blade signature
but are not located at the same position as the blade at the current time step. Due
to the fact that the rotation of the wake is directed opposite to that of the rotor, the
signature of the blade is transported with the wake rotation and at 0.5 D there is an angle
difference of $15°$ between blade position and blade signature. This angle lag increases
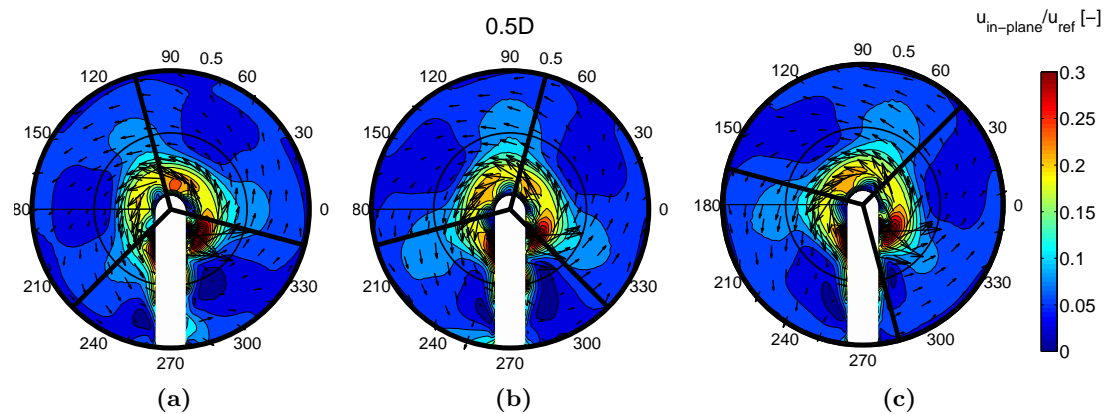with downstream distance, as the wake and rotor continue their rotation in opposite
directions.

Figure 3.33: Contours of in-plane velocities components at different rotor positions $-15°$ (a),
$15°$ (b), $30°$ (c) at a plane 0.5 D downstream. The lines depict the rotor and the tower is
represented in white.

3.2 Yawed Inflow

Yawed inflow of $30°$ relative to the rotor's axis of rotation is examined to quantify the
effect of yaw on the near wake. In CFX, simulations of inflow which is not circumferen-
tially uniform must be carried out as unsteady simulations. The larger the angle between
the inflow direction and the axis of rotation, the larger is the error in the simulations.
Therefore, no steady state analysis can be performed for simulating yawed inflow and
consequently the unsteady analysis has to be carried out without a uniform flow as initial
conditions.

The simulation options for the unsteady runs with yaw are summarized on table 3.10.
Only one time step per degree of revolution and 3 coefficient loops per timestep were
chosen to reduce computational time, as reaching convergence without valid initial con-
ditions is a time consuming process for unsteady simulations. The system of coordinates
used for yaw and the operating conditions are the same as in the MEXICO, where yaw
was also studied. The yawed coordinate system is rotated by $-30°$ around the Y-axis,
so that the X_{yaw} axis is parallel and opposite to the incoming yawed wind (Fig. 3.34a).

The tip-speed ratio at which the wind turbine operates, is $\lambda = 6.67$, using the velocity in the direction of the yawed coordinate system.

total time [s]	0.1413
time per timestep [s]	3.9×10^{-4}
timesteps per degree of revolution [ts/°]	1
coefficient loop iterations	3

Table 3.10: Solver setup for the unsteady simulation in yaw.

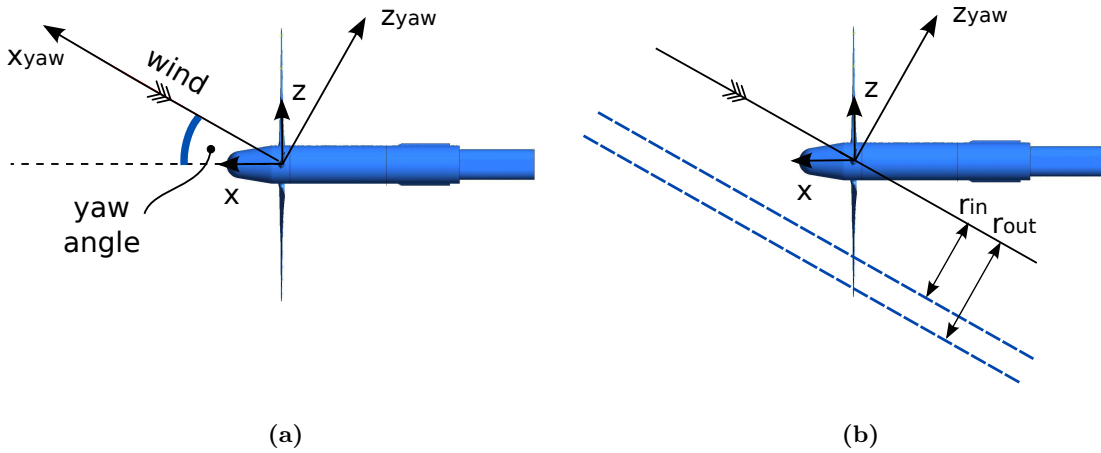(a)   (b)

Figure 3.34: Coordinate system for simulation in yaw (a) and position of axial traverses for comparison with experiment (b)

Periodicity of the unsteady yaw results is confirmed by monitoring the pressure and velocity components at different downstream distances, as the rotor position is changing by 1° per timestep. The pressure values vary periodically every 120°. The values at two points located 0.1 D and 0.3 D downstream of the rotor, over two different periods, overlap with an accuracy of 0.47% and 0.43% of the dynamic head of the flow ($dh = 1/2\rho u_{ref}^2 = 133.3$ Pa) (Fig. 3.35b). Further downstream, at 0.5 D the amplitude of the oscillation is reduced but the periodicity is still visible, and the periods overlap with an accuracy of 0.03%dh. The velocities also oscillate with the same period and the difference between two blade crossings is 0.03% u_{ref} at 0.5 D. The absolute velocity at this point is on average 54% u_{ref}, so the difference is relatively negligible. The values presented in the following comparison with experiments are averaged over one rotor revolution. Finally, for this setup the quality decreases beyond 1.5 D.

Apart from the pressure and the velocity, periodic fluctuations are also observed on the torque exerted on the rotor. As the rotor rotates, each blade experiences different incidence angles depending on its position. Since the rotor has a finite number of blades this also affects the torque that acts on the rotor at every timestep. The fluctuations are periodic for every 120° of rotation (Fig. 3.36). The average torque is 65 Nm lower
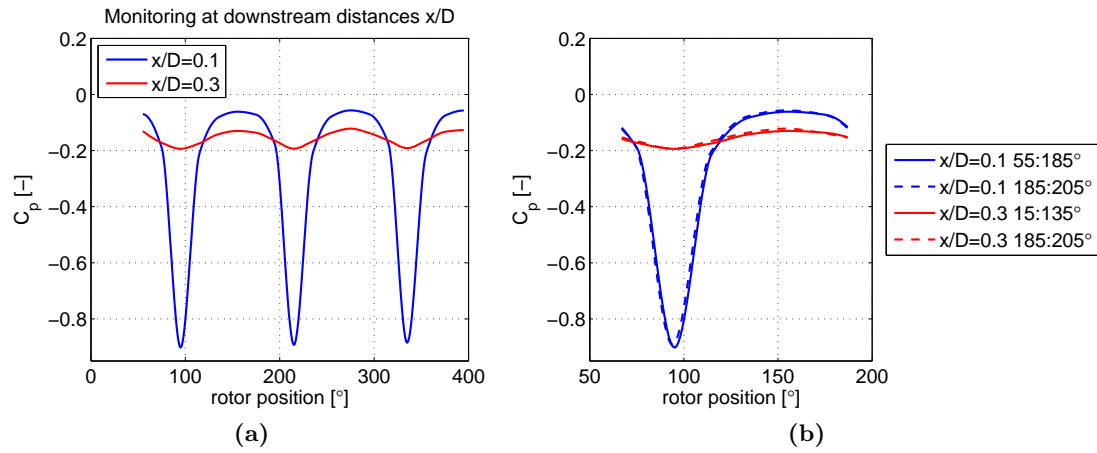
Figure 3.35: Periodic variation of the pressure at two downstream positions (a) and overlap of two subsequent periods (b), for yawed inflow.
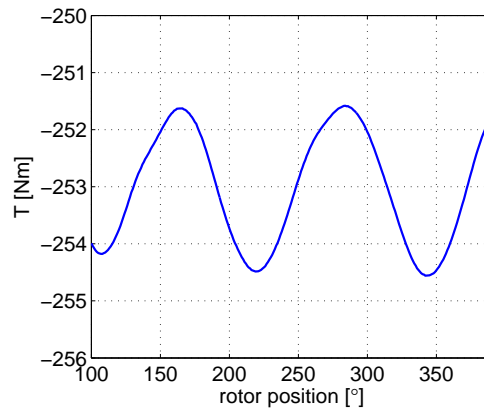
Figure 3.36: Periodic variation of the torque acting on the rotor operating in yawed inflow.

than for the uniform inflow, which is a deficit of 20% relative to the torque calculated for uniform conditions. Compared to the experiments, the predicted torque is 13% higher than the measured value. The thrust on the rotor is on average 1700 N, so 10% lower than the thrust with uniform inflow.

3.2.1 Near Wake

Induced velocity

The results of the MEXICO experiment for yawed inflow include tracking of the velocity components along axial traverses, as in the case of the axis-parallel inflow conditions. The

velocity components are specified in the yawed coordinate system so that the maximum possible velocity is 15 m/s. Results from the CFD study show an average difference of 7% u_{ref} for all velocity components. The smallest error is found for the axial components at 5% u_{ref} and the largest for the radial component, w, at 9.7%. u_{ref}. At the rotor plane the induced axial velocity is 75% u_{ref} (Fig. 3.37).
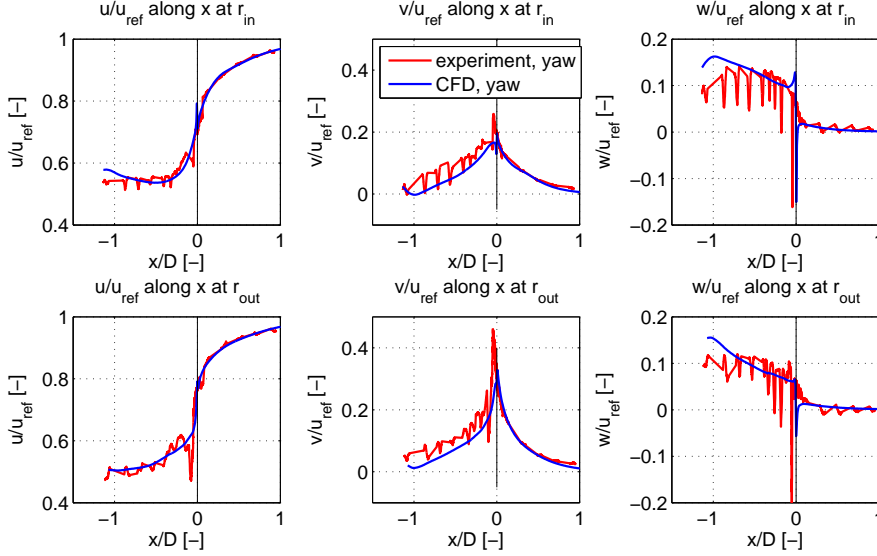
Figure 3.37: Comparison of the estimated velocity components with experiment along two axial traverses for yawed inflow.

Velocity deficit and wake width

The velocity deficit in the wake of the rotor in yaw is 20% smaller than when the turbine operates in uniform inflow. This is to expected, as the wind turbine is not operating at its optimum point and the power extracted is less than in the ideal case. Furthermore, the wake is skewed by a skew angle, χ, which is larger than $\gamma = 30°$ (Fig. 3.38a). According to the formula proposed by Burton et al. [7], which is a simplified form of Eq. 1.17, the wake skew angle χ can be approximated based on the yaw angle, γ and the axial induction factor a as

$$\chi = (0.6a + 1)\gamma \tag{3.7}$$

For the current case this results in $\chi = 34°$, which is an underestimation of the wake skew by 2°, as an angle of $\chi = 36°$ is derived from the simulations. Moreover, a smaller wake expansion is observed in the yawed than in the uniform case at the same tip-speed ratio. For the uniform inflow conditions, the wake expands to 134% D, whereas when operating in yaw only an expansion until 114% D is observed. The expansion is non-uniform, as the wake is partly obstructed by the presence of the nacelle.
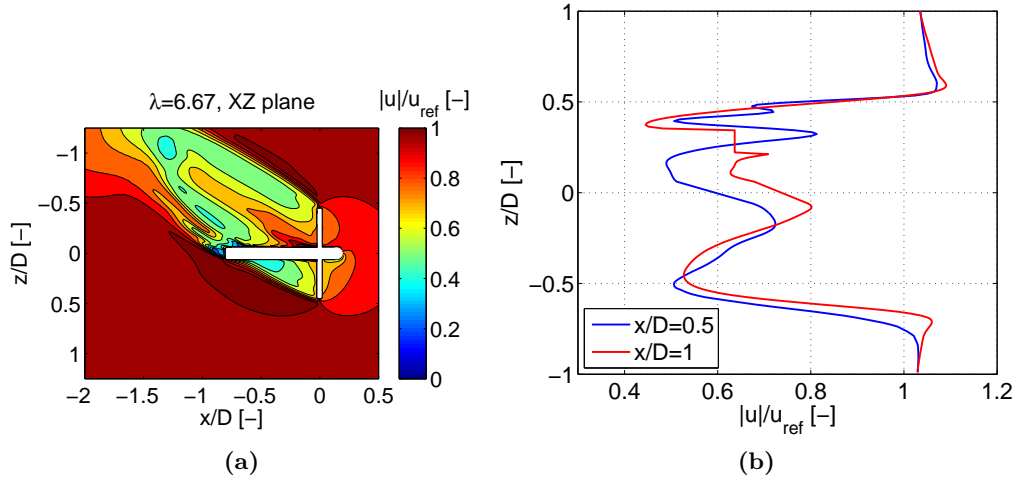
Figure 3.38: Contours of velocity deficit in the XZ plane (a) and velocity deficit profile at two downstram distances (a).
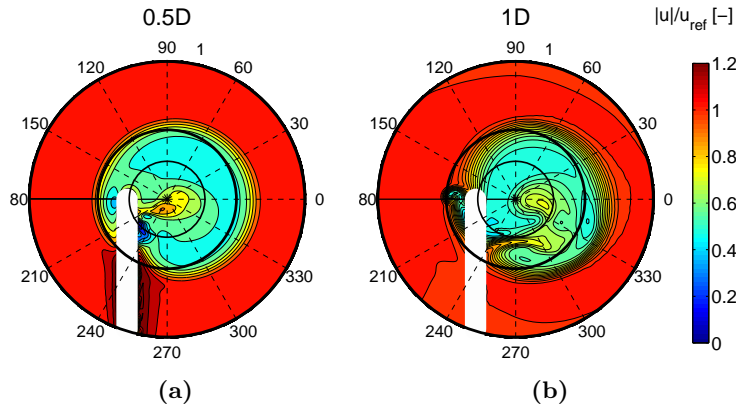
Figure 3.39: Velocity deficit at two downstream distances at a plane of radius $r = 1\,\mathrm{D}$.

Looking at the flowfield downstream of the rotor one can see that the wake develops normal to the axis of the rotor rather than to the direction of the incoming wind, as at cross sections parallel to the axis of rotation the wake maintains a circular form. Moreover, velocity contours at different downstream positions help visualize the wake deflection. Only contours up to $1\,\mathrm{D}$ are presented due to the coarsening of the mesh beyond $1.5\,\mathrm{D}$. Within the near wake a Gaussian distribution of the velocity deficit within the wake width is not applicable. A top-hat distribution might be more suitable, or alternatively a Gaussian distribution with the superposition of a function which has its maxima at the edge of the wake and the minimum at its middle. The superposition function should decay with downstream distance and the wake assumes the typical far-wake bell form.

Flow angles

When the wind turbine is operating in yawed inflow ,non-axisymmetric distribution of flow angles is expected. For all considerations, the basic yaw angle of 30° of the incoming flow is subtracted from the in-plane yaw angle to help visualize the in-plane angles and the impact of the turbine on the flow under such flow conditions. In the case of uniform inflow the pitch and yaw angles are similarly distributed on the plane, resulting in uniform radial and tangential velocities on the plane. This is, however, not the case when the flow is not axial, as each blade experiences temporally varying incidence angles and at each position deflects the flow differently. Furthermore, the nacelle interacts highly with the wake and introduces additional non-uniformity, as it acts like a blunt body positioned crosswise in the wake. This is visible in the large yaw angles at $x/D = 1$, where the nacelle ends and its own wake influences the rotor's wake (Fig. 3.38a).

Compared to uniform inflow, all values show a larger deviation over the cross sectional plane. Whereas in uniform inflow the flow angles decay with downstream distance, the angles at $1\,$D are here on average 4° larger than at $0.5\,$D, due to the interaction with the nacelle's wake. As in reality the nacelle length to rotor radius ratio is much smaller, results up to $0.5\,$D represent in this case the reality more closely (Table 3.11). The non-uniform distribution of the pitch and flow angles results in a non-circular wake rotation, as seen in the distribution of the in-plane vectors (Fig. 3.41). While a rotation of the wake in the counter-clockwise direction is visible, the rotation is not circular and not symmetric. Finally, while the wake is displaced to the right along the lateral Z-axis no displacement occurs in the vertical direction, despite the non-uniform flow (Fig. 3.39).

	0.5D, yaw		1D, yaw	
	μ	σ	μ	σ
u_{axial}/u_{ref}	58%	12%	56%	9%
u_{rad}/u_{ref}	2.3%	9.3%	0.24%	12.7%
u_{tan}/u_{ref}	10%	9.2%	7.6%	9.3%
yaw angle [°]	-3	11.5	-5.8	9.6
pitch angle [°]	3	11.5	8.48	8.12

Table 3.11: Mean values, μ, and standard deviations, σ, of the flow properties at $0.5\,$D downstream of the turbine.

Vorticity

The vortices shed by the rotor in the yawed flow are transported with the wake in the direction of the skewed freestream flow. However, just as the wake, the trajectories of the vortices are also skewed by an additional angle of approximately 6°. This effect is
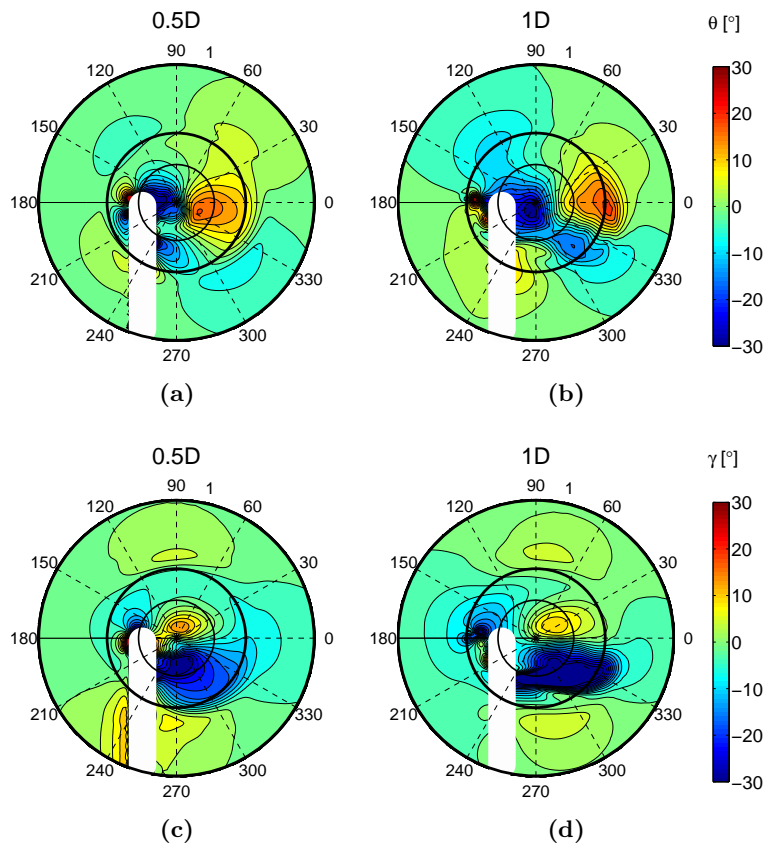
Figure 3.40: Contours of pitch (a), (b) and yaw angles (c), (d) at 0.5 D and 1 D.
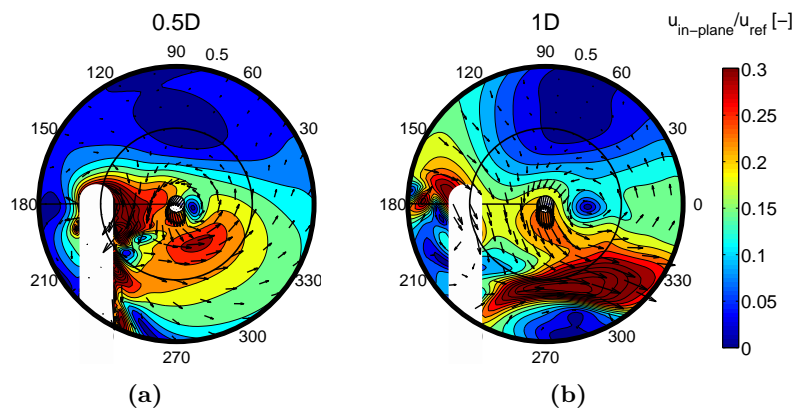
Figure 3.41: Contours of in-place velocity components at different rotor positions at 0.5 D and 1 D downstream.

seen on (Fig. 3.42a), which shows an XY-plane rotated by $30°$. In this plane the vortex appears to decay already at $1\,D$ downstream distance, which is not the case, as is seen on the XZ-view. (Fig. 3.42b) The vortex pitch between two subsequent helical vortex structures is $0.3\,D$, which is $0.1\,D$ smaller than in the non-skewed case where $p_v = 0.39\,D$. This is caused by the fact that the vortices are squeezed together in a shear motion as the wake is skewed (Fig. 3.43).

Close to the hub two vortex structures form. Around the hub there is the hub vortex, as in the uniform case, but its strength decreases very quickly with downstream distance (Fig. 3.42b). The hub vortex mainly separates from the hub at $0.25\,D$ and is transported downstream with the wake. The remaining hub vortex, which continues its rotation around the nacelle trails off at its edges and mixes with the rest of the wake, resulting in the large inflow angles at $1\,D$, as observed in the section concerning flow angles.

Figure 3.42: Contours of non-dimensionalized vorticity for turbine operating under $30°$ yaw.

Figure 3.43: Isosurface of vorticity for $30°$ yawed inflow colored by velocity.

Chapter 4

Future Work

Further work by using the computational setup and results derived from this project could complement the current results and provide additional information about the wake characteristics. More specifically, the following topics could be studied:

- Provided the computational setup and mesh generation options, yawed inflow under different inflow angles can be simulated. A range of $15, 30, 45°$ would provide a complete set of yaw simulations. Different tip-speed ratios could also be examined for different inflow angles.

- Using a setup and domain with mesh which already exist, the effect of shear can be simulated in unsteady simulations. Steady-state simulations present similar problems for the case of shear, as for yaw. Initial conditions have already been simulated but further convergence is required as periodicity is not reached.

- For studying shear and ground-turbine interaction, a ground surface could be included in the setup, as currently shear can only be simulated by using a shear velocity profile.

- A correlation of the different inflow conditions to the near wake should be derived for different operating conditions to facilitate the generation of velocity profiles to be used in far wake models.

Chapter 5

Conclusion

The goal of this project was to study the wake aerodynamics and create a modeling database for the flow values within the near wake, up to a distance of two rotor diameters, $2\,\mathrm{D}$ downstream of the rotor plane. Detailed knowledge of the characteristics of the flow at that position can be used for the development of far wake models which use the near wake flow as boundary conditions at the most upstream position.

Advantages of such models for the far wake are that the computationally intensive rotor plane must not be resolved as would be the case for full rotor simulations, and that more realistic values than a simpified bell-shaped or top-hat profile can be used. It is, however, necessary to first gain understanding of the flow properties in the near wake, by performing full rotor simulations at different operating points. Furthermore, high-resolution and reliable full rotor simulations of an entire wind turbine, in uniform and non-uniform inflow conditions, can be used to compare with measurements and provide more complete information about the flow than experiments in controlled conditions.

- Full rotor simulations, were performed using the commercial software ANSYS CFX 12.1. Steady-state simulations with and without the tower were carried out in uniform inflow conditions, at different tip speed ratios of $\lambda = 4.17, 6.67$ and 10. Unsteady simulations were carried out at $\lambda = 4.17$ for uniform inflow, to resolve unsteady behavior that occurs due to increased separation at that tip-speed ratio. Non-uniformity in the inflow was studied for $30°$ yawed inflow at the optimum operating point $\lambda = 6.67$.

- Results show good agreement with measurements obtained by the MEXICO experiment, carried out in controlled conditions by the Energy Reasearch Center of the Netherlands. The prediction of the induced velocity matches with an accuracy of 4% of the reference speed. The thrust on the turbine is predicted with an accuracy of 3.5% while the values for the torque are overestimated by 10% approximately. For yawed inflow, the difference is larger but remains in the same range, with an average difference of $5\% u_{ref}$ in the predicted induced velocity. The estimated

torque is on average 13% higher than the torque measured in experiments.

- Simulations of uniform inflow show large non-uniformity introduced by the presentce of the tower, which results in an increase of turbulence intensity by approximately 0.1% at 1 D downstream distance. The turbulence intensity is reduced by half at 2 D. The largest centerline velocity deficit is found for $\lambda = 4.17$, but the average velocity deficit is smallest at that tip-speed ratio when comparing axial velocity averagd over a rotor plane at 2 D. The wake width at 2 D increases linearly with increasing tip speed ratio.

- The angular induction factor is estimated to be about 0.015 for $\lambda = 6.67$. The angular induction factor increases with increasing tip-speed ratio, as tangential velocity is distributed more uniformly across the rotor plane. The in-plane velocities and flow angles are significantly affected by the presence of the tower at 2 D, which causes a 5% less uniform distibution due to interaction of the tower and rotor wake.

- Vorticity strength increases with increasing tip-speed ratio, but the distance that a tip vortex is transported during one rotor revolution decreases as the tip-speed ratio increases. For tip-speed ratio $\lambda = 10$, the three single tip vortices merge into one vortex sheet after one revolution.

- Unsteady results at $\lambda = 4.17$ show better agreement with experiments at traverses directly downstream of the rotor, with an overall difference of 0.4% u_{ref} between the predicted induced velocity components and measurements. Accuracy is similar to steady-state results for the predicted induced velocity at larger downstream distances, as regions far from the rotor are not dominated by unsteady effects of flow separation occuring at the blades.

- Results of the turbine operating in 30° yawed inflow show a periodic oscillation of the torque acting on the rotor, which is on average 20% lower than the torque exerted at uniform inflow conditions. Comparison with the experiments shows good agreement in the predicted induced velocity. The predicted deviation of the wake is 36°. The angle is larger than the approximation proposed by Burton et al. [7] by 2°. The skewed wake is largely non-uniform, both in the distribution of the velocity deficit as well as the flow angles, so that a bell-shaped or Gaussian velocity deficit profile would be by no means a realistic modeling assumption. Concerning the tip and hub vortices, the distance that a vortex is transported during one rotor revolution is smaller by 0.1 D compared to the case of uniform inflow, as the vortices are squeezed together as a helix under shear. The hub vortex detaches from the nacelle and follows the direction of the wake, causing additional non-uniformity in the wake.

Results have shown that non-uniformity in the near wake is not negligible, even when the inflow is uniform. In-plane tangential velocity components are of the order of 10% u_{ref}. The radial component could, however, be neglected as its value is approximately

two orders of magnitude lower than the tangential component. Wake non-uniformity in non-uniform inflow is much more pronounced, and even radial components are not negligible. Interaction with structures of the wind turbine, such as the nacelle and tower also increases in yawed inflow as does the interaction between the wake and the vortices.

Bibliography

[1] U.S. Energy Information Administration. International energy statistics. http://www.eia.gov/cfapps/ipdbproject/IEDIndex3.cfm, 2011.

[2] J. F. Ainslie. Calculating the flowfield in the wake of wind turbines. *Journal of wind engineering and industrial aerodynamics*, 27, 1988.

[3] R. J. Barhtelmie, L. Folkerts, G. C. Larsen, K. Rados, S. C. Pryor, S. T. Frandsen, B. Lange, and J. G. Schepers. Comparison of wake model simulations with offshore wind turbine wake profiles measured by sodar. *Wind Energy*, 12:431–444, 2009.

[4] R. J. Barthelmie, K. Hansen, S. T. Frandsen, O. Rathmann, J. G. Schepers, W. Schlez, J. Phillips, K. Rados, A. Zervos, E. S. Politis, and P. K. Chaviaropoulos. Modelling and measuring flow and wind turbine wakes in large wind farms offshore. *Wind Energy*, 12:431–444, 2009.

[5] A. Bechmann, N. Sørensen, and F. Zahle. CFD simulations of the MEXICO rotor. *Wind Energy*, 14:677–689, 2011.

[6] K. Boorsma and J. G. Schepers. Model experiments in controlled conditions. Technical report, Energy Research Center of the Netherlands, 2009.

[7] T. Burton, D. Sharpe, N. Jenkins, and E. Bossanyi. *WInd Energy Handbook*. John Wiley & Sons, 2001.

[8] J. W. Cleijne. Results of sexbierum wind farm; single wake measurements. Technical report, TNO Institute of Environmental and Energy Technology, 1993.

[9] R. P. Coleman, A. M. Heingold, and C. W. Stempin. Evaluation of the induced-velocity field of an idealized helicopter rotor. *NACA ARR No. L5E10.*, 1945.

[10] Global Wind Energy Council. Global wind report. Technical report, 2010.

[11] A. Crespo, J. Hernández, and S. Frandsen. Survey of modelling methods for wind turbine wakes and wind farms. *Wind Energy*, 2:1–24, 1999.

[12] P. R. Ebert and D. H. Wood. The near wake of a model horizontal-axis wind turbine, part II: General features of the three-dimensional flowfield. *Renewable Energy*, 18:513–534, 1998.

[13] D. M. Eggleston and F. S. Stoddard. *Wind Turbine Engineering Design.* Van Nostrand Reinhold Company, 1987.

[14] S. Frandsen. On the wind speed reduction in the center of large clusters of wind turbines. *Journal of wind engineering and industrial aerodynamics*, 39, 1992.

[15] E. Hau. *Wind Turbines - Fundamentals, Technologies, Application, Economics.* Springer, 2nd edition, 2006.

[16] S. Jafari, N. Chokani, and R. S. Abhari. An immersed boundary method for efficient simulation of wind flow over complex terrain. *Journal of Solar Engineering*, 134, 2012.

[17] P. Jenny and L. Kleiser. Turbulent flows. Lecture Notes, ETH Zurich, 2010.

[18] N. O. Jensen. A note on wind generator interaction. Technical report, Risoe National Laboratory, Roskilde, Denmark, 1983.

[19] A.L. Rogers J.F. Manwell, J.G. McGowan. *Wind Energy Explained - Theory Design and Application.* John Wiley & Sons, 2002.

[20] B. Lange, H. P. Waldl, A. G. Guerrero, and D. Heinemann. Modelling of offshore wind turbine wakes with the wind farm program flap. *Wind Energy*, 6:87–104, 2003.

[21] G. Leishman. Challenges in modelling the unsteady aerodynamics of wind turbines. *Wind Energy*, 5:85–132, 2002.

[22] P.J. Moriarty and A.C. Hansen. Aerodyn theory manual. Technical report, NREL/EL-500-36881, 2005.

[23] CFD Online. SST k-omega model. `http://www.cfd-online.com/`, April 2012.

[24] B. Sanderse. Aerodynamics of wind turbine wakes. Technical report, Energy Research Center of the Netherlands, 2009.

[25] J. G. Schepers. ENDOW: Validation and improvement of ECN's wake model. Technical report, Energy Research Center of the Netherlands, 2003.

[26] J. G. Schepers and H. Snel. Model experiments in controlled conditions. Technical report, Energy Research Center of the Netherlands, 2007.

[27] L.J. Vermeer, J.N. Sørensen, and A. Crespo. Wind turbine wake aerodynamics. *Progress in Aerospace Sciences*, 39:467–510, 2003.

[28] S. G. Voutsinas, K. G. Rados, and A. Zervos. Wake effects in wind parks. a new modelling approach. *Proc. European Community Wind Energy Conference.*, pages 447–447, 1993.

[29] J. Whale, C. G. Anderson, R. Barreiss, and S. Wagner. An experimental and numerical study of the vortex structure in the wake of a wind turbine. *Journal of wind engineering and industrial aerodynamics*, 84:1–21, 2000.

[30] D. C. Wilcox. *Turbulence Modeling for CFD.* DCW Industries, Inc., 1994.

[31] D. H. Wood. Simple equations for helical vortex wakes. *Journal of Aircraft*, 31:994–995, 1994.

Title of work:

Numerical Study of Wind Turbine Wake Aerodynamics in Uniform and Yawed Inflow

Thesis type and date:

Master Thesis, April 2012

Supervision:

Samira Jafari

Student:

Name:	Christina Tsalicoglou
E-mail:	ctsalico@student.ethz.ch
Legi-Nr.:	07-925-936
Semester:	10